Lagrangian investigation of the interface dynamics in single-mode Rayleigh-Taylor instability

Dongxiao Zhao (赵东晓),[1] Lanlan Xiao (肖兰兰),[2] Hussein Aluie,[3] Ping Wei (韦萍),[4] and Chensen Lin (林晨森)[5,*]

[1]*School of Naval Architecture, Ocean and Civil Engineering, Shanghai Jiao Tong University, Shanghai 200240, China*

[2]*School of Mechanical and Automotive Engineering, Shanghai University of Engineering Science, Shanghai 201620, China*

[3]*Department of Mechanical Engineering, University of Rochester, Rochester, New York*

[4]*School of Aerospace Engineering and Applied Mechanics, Tongji University, Shanghai 200092, China*

[5]*Artificial Intelligence Innovation and Incubation Institute, Fudan University, Shanghai 200433, China*

(Dated: August 30, 2023)

Abstract

We apply Lagrangian particle tracking to the two-dimensional single-mode Rayleigh-Taylor (RT) instability to study the dynamical evolution of fluid interface. At the onset of the nonlinear RT stage, we select three ensembles of tracer particles located at the bubble tip, at the spike tip, and inside the spiral of the mushroom structure, which cover most of the interfacial region as the instability develops. Conditional statistics performed on the three sets of particles and over different RT evolution stages, such as the trajectory curvature, velocity, and acceleration, reveals the temporal and spatial flow patterns characterizing the single-mode RT growth. The probability density functions of tracer particle velocity and trajectory curvature exhibit scalings compatible with local flow topology, such as the swirling motion of the spiral particles. Large-scale anisotropy of RT interfacial flows, measured by the ratio of horizontal to vertical kinetic energy, also varies for different particle ensembles arising from the differing evolution patterns of the particle acceleration. In addition, we provide direct evidence to connect the RT bubble re-acceleration to its interaction with the transported fluid from the spike side, due to the shear driven Kelvin-Helmholtz instability. Furthermore, we reveal that the secondary RT instability inside the spiral, which destabilizes the spiraling motion and induces complex flow structures, is generated by the centrifugal acceleration.

* linchensen@fudan.edu.cn

I. INTRODUCTION

When a light fluid accelerates against or supports a heavy fluid, the perturbed interface between these two fluids is subjected to the Rayleigh-Taylor (RT) instability [1, 2], which could lead to the formation of bubbles and spikes, and finally to turbulence at high Reynolds numbers [3]. RT instability has important consequences in many natural and engineering applications, such as the fingering structures of supernova explosion remnants [4] in astrophysics, the fusion target degradation in the acceleration and deceleration stages of inertial confinement fusion [5–9], the breakup and atomization of diesel and gasoline sprays in automotive engines [10], and the coastal upwelling phenomenon in ocean dynamics [11]. Theoretical, experimental, and numerical investigations on RT instability have been performed for decades to advance the fundamental understanding of this subject, as summarized by several recent reviews [3, 12–15].

Despite extensive research efforts, many problems in RT flows remain unresolved even in the single-mode configuration, in which the initial perturbation contains only a single sinusoid, due to the inherent nonlinearity and also due to the complexity induced by viscosity, compressibility, surface tension, mass ablation, and stratification [16–22]. According to Wei and Livescu [16], the evolution of two-dimensional (2D) high Reynolds number single-mode RT can be divided into five stages: diffusive growth (DG), exponential growth (EG), potential flow growth (PFG), reacceleration (RA), and chaotic development (CD). In the diffusive growth stage, diffusional effect governs the system and sharp interfaces are rapidly smeared out for miscible fluids. In the exponential growth stage, RT development follows the linear stability theory with a constant growth rate $\gamma = \sqrt{\mathcal{A}kg}$, where $\mathcal{A} = \frac{\rho_h - \rho_l}{\rho_h + \rho_l}$ is the Atwood number with ρ_h, ρ_l the heavy and light fluid densities, $k = 2\pi/\lambda$ is the perturbation wavenumber (λ is the wavelength), and g is the gravitational acceleration. As the magnitude of the instability exceeds 0.1λ, the exponential growth terminates and nonlinear effect dominates, where the uprising bubble and the sinking spike become apparent. The system then transits to the potential flow growth stage with constant bubble and spike velocities, which is well predicted by the potential flow theory [23–26] or the buoyancy-drag model [27]. In the reacceleration stage, the bubble (and also the spike) velocity increases again, which is attributed to the vortices induced by the Kelvin-Helmholtz instability near the fluid interface and advected to the bubble tip [16, 17, 28]. Ref. [29] derived an expression for

the effective drift imparted by these vortices on the large scale flow. Ref [17] also showed that the reacceleration is dependent on the perturbation Reynolds number Re_p and Atwood number $\mathcal{A}$, and provided a phase diagram for RT reacceleration. Finally, if the system Reynolds number is high enough, single-mode RT growth can lead to the chaotic mixing stage [3, 30].

The above evolution process is altered in varying degrees of viscosity and compressibility, which modifies the RT growth rate as well as the energy and enstrophy budgets [31]. Hu et al. [32] investigated the single-mode RT bubble velocity and vorticity at different viscosity levels (or Reynolds numbers), and proposed a linear relationship between bubble-tip vorticity and viscosity in the reacceleration stage by a least square fit. After the bubble reacceleration, if viscous effect is prominent, an alternating deceleration-acceleration pattern will emerge, due to the combined effects of viscous-inhibition and shear-generation of vorticity near the bubble tip. Wieland et al. [33] studied the compressibility effects on the vorticity dynamics of 2D single-mode RT at low Atwood numbers. They found that stronger stratification (larger Mach number) leads to more symmetric growth of bubbles and spikes, but the level of vorticity as well as the bubble reacceleration is suppressed. By examining the individual budget terms in the vorticity transport equation, the authors concluded that the baroclinic torque dominates vorticity generation, which diminishes at high stratification levels and thus RT is suppressed when Mach number is large. Similar conclusion is also drawn in Luo et al. [22], who investigated the compressibility effects on both low and high Atwood number single-mode RT, and distinguished the stabilization effects of initial density stratification from the expansion-compression effect. Fu et al. [34, 35] modified the buoyancy-drag model to account for the compressibility effect in single-mode RT, and found the critical Atwood number 0.25 at which nonlinear saturation of bubble growth is realized at various Mach numbers. They further found that the acceleration of the heavy fluid in front of bubble tip is nearly constant, and numerically verified a scaling law $\mathcal{A}^{2.5}\mathcal{M}^2$ for this acceleration, where $\mathcal{M}$ is the Mach number.

In addition to the above effects, many of the complexities in RT flows are due to the secondary Kelvin-Helmholtz (KH) instability, which boosts the spiral structure between the bubble and spike, accelerates the bubbles, and enhances fluid mixing. Olson et al. [36] numerically studied the early nonlinear stage of multi-mode RT flows with imposed shear rates, which leads to a combined RT/KH instability growth. Contrary to the predictions by linear

theory, in which the instability growth rate is enhanced by the addition of shear, numerical results show that a small amount of imposed shear rate in fact decreases the growth, while a large shear rate enhances the instability. By visual inspection and quantitative analysis, the suppression of instability at low shear levels is due to a small amount of energy being channeled into vertical mixing, while the contrary is true for a high shear rate. Chen et al. [37] numerically investigated the coupled single-mode RT-KH instability system with a discrete Boltzmann model. They found that RT effect dominates the late stage development, while in the early stage the dominant mechanism depends on the relative strength between buoyancy and shear. The total boundary length of the temperature fields in the pure RT and KH simulations can help discriminate the dominant mechanism of the coupled RT and KH system. Hamzehloo et al. [38] performed a parametric study of RT flows with surface tension, and found that surface tension prevents the formation of KH type vortices especially at high Reynolds numbers. With increasing Reynolds number, the amount of KH vortices as well as the interfacial area increases, but the penetration depths of bubble and spike remain constant, which depend primarily on the Atwood number.

An effective yet relatively under-explored way to study fluid mixing and interfacial flows is the Lagrangian approach [39–42], which, however, is seldom applied to the RT problem. Despite a few studies on particle-induced RT instability [43–45] in which the RT growth rate, particle concentration and mixing are investigated, the Lagrangian passive particle tracking, to the best of our knowledge, has never been reported with the exception of reference [18]. In that work, the authors studied single-mode RT using the discrete Boltzmann method with three types of tracers marking the heavy fluid, the light fluid, and the interface. RT mixing is quantified by the tracer defined local mixedness, and the secondary KH instability is featured by the abrupt increase in vertical-averaged mixedness. Viscosity and compressibility on RT mixedness show two-stage effects due to the formation of large scale structures at the early stage, and the generation of small structures at later stages. Although reference [18] sheds some light on the RT interfacial evolution and mixing using tracer particles, several important features unique to the Lagrangian description remain to be explored, such as statistics on particle velocity, acceleration, and trajectory curvature, as we shall study in this paper. These quantities can on one hand reflect characteristic flow kinematics such as the oscillatory trajectories of particles trapped in coherent vortices, and on the other hand they can be adopted to explain important flow dynamic behavior like bubble reacceleration

in single-mode RT as discussed in later sections.

The current paper focuses on Lagrangian investigation of single-mode RT's interfacial growth and mixing, and aims to provide an alternative way to reveal different evolution stages of 2D single-mode RT, which gains deep physical insights into this complex flow. To this end, we seek to address the following questions: (i) How does the single-mode RT interface evolve in space and time? (ii) What statistical quantities govern the interfacial dynamics, and how does the statistics differ at different regions of single-mode RT, i.e., the bubble, the spike, and the spiral regions? (iii) Why does single-mode RT develop directional anisotropy between the horizontal and vertical components? Answers to the above questions will deepen our understanding of single-mode RT physics in two dimensions, and also lays a basis for the Lagrangian investigation of more complicated multi-mode turbulent RT flows. For example, detailed geometric information of the interface avails many predicative models of bubble and spike growth of single-mode RT in the highly nonlinear stage [26], while the interfacial dynamics controls many physical and chemical processes occurring at the interface, such as mass ablation in inertial confinement fusion and fuel/oxidizer mixing and reaction in combustion chambers [46].

In the following, we first provide details on the numerical simulation of RT flows and the Lagrangian tracking approach. Next, we perform statistical analysis on Lagrangian velocity, acceleration, curvature, etc., focusing on different stages and different regions of single-mode RT. We then study the large-scale anisotropy associated with the horizontal and vertical kinetic energies, and finally present summaries and conclusions of our discussions.

II. GOVERNING EQUATIONS AND NUMERICAL IMPLEMENTATION

We adopt the compressible two-component Navier-Stokes equations to describe the RT instability, which consists of the conservation equations of the mass fraction, mass, momentum, and energy [22, 32]:

$$\frac{\partial \rho Y_i}{\partial t} + \partial_j(\rho u_j Y_i) = \partial_j(\rho D \partial_j Y_i) \tag{1}$$

$$\frac{\partial \rho}{\partial t} + \partial_j(\rho u_j) = 0 \tag{2}$$

$$\frac{\partial \rho u_i}{\partial t} + \partial_j(\rho u_i u_j) = -\partial_i P + \partial_j \tau_{ij} - \rho g \delta_{iz} \tag{3}$$

$$\frac{\partial \rho E}{\partial t} + \partial_j((\rho E + P)u_j) = \partial_j(\tau_{ij} u_i) - \rho u_i g \delta_{iz} + \partial_j(\kappa \partial_j T) \tag{4}$$

where ρ, u_i, P, g are density, velocity, pressure, and the gravitational acceleration, respectively, Y_i is the mass fraction of the i-th component (i=1,2), and $E = \frac{1}{2}u^2 + c_v T$ is the total energy density, in which c_v is the specific heat at constant volume and T is the temperature. $\tau_{ij} = 2\mu(S_{ij} - \frac{1}{d}S_{kk}\delta_{ij})$ is the viscous stress tensor and d is the spatial dimension, $S_{ij} = (\partial_i u_j + \partial_j u_i)/2$ is the strain rate tensor, while μ, D, κ are the dynamic viscosity, mass diffusivity, and thermal conductivity, respectively. The above set of equations is complemented by the ideal gas equation $P = \rho\widetilde{R}T(Y_1/W_1 + Y_2/W_2)$, where $\widetilde{R}$ is the universal gas constant, W_1, W_2 are the molecular weights of the two species. Note that we have not included the enthalpy of formation and also ignored the enthalpy diffusion term in the total energy equation, since we set equal molecular weights $W_1 = W_2$ in our RT simulations, and thus the effects of enthalpy diffusion can be neglected [47]. Due to the constraint $Y_1 + Y_2 = 1$, only one of the two mass fraction equation (1) is required for numerical simulation. In addition, by setting equal molecular weights $W_1 = W_2 = W$, the ideal gas equation of state reduces to $P = \rho\frac{\widetilde{R}}{W}T$, and the mass fraction equation (1) is thus decoupled from other equations. Here we include the mass fraction equation merely to track the fluid interface. For general situations with unequal molecular weight $W_1 \neq W_2$, the physics remains unchanged when the ratio W_2/W_1 is close to 1, as we have observed in a $W_2/W_1 = 2$ case whose result shares similar RT physics as in the equal molecular weight case (Appendix A). In more complex situations where combustion or general chemical reactions are included, this set of equations is still applicable by adding the chemical source term and enthalpy diffusion, as we shall explore in our future work.

We conduct 2D single-mode RT simulations using the DiNuSUR code, which is a hybrid pseudo-spectral and six-order compact finite difference solver to account for both the homogeneous and the inhomogeneous directions, and fourth order Runge-Kutta scheme is used for time integration. The code has been applied to both single- and multi-mode RT systems in previous studies [17, 48, 49], and here we have implemented the Lagrangian particle tracking using cubic spline for spatial interpolation and second order predictor-corrector scheme for time advancing. The Lagrangian module can be applied both online (simultaneously with the Eulerian time advancing) and off-line (by post-processing). For Lagrangian tracking as a post-processing step, the Eulerian snapshots should be saved densely in time to satisfy the Courant-Friedrichs-Lewy (CFL) condition [50] $\max(u_x\Delta t, u_z\Delta t)/\Delta x \leq 1$, where Δt is the time interval between two consecutive snapshots, and Δx is the grid size assumed to be

uniform.

As for the boundary condition, the horizontal boundaries are periodic, while the top and the bottom boundaries are assumed to be no-slip walls, in which the conditions $\frac{\partial T}{\partial z} = 0$, $\frac{\partial Y_i}{\partial z} = 0$, $\frac{\partial P}{\partial z} = -\rho g$ are imposed. For the initial conditions, we impose uniform heavy fluid of density ρ_h on top half and uniform light fluid of density ρ_l at the bottom half, and the initial pressure field satisfies the hydrostatic equilibrium condition $\partial P/\partial z = -\rho g$. The mass fraction field follows from the density field. Initial perturbation is imposed on the velocity field as a small amplitude cosine wave. More details on the initial density, pressure, and temperature profiles, as well as the precise initial perturbation is shown in Appendix B.

Here we perform three single-mode RT simulations at low, middle, and high Atwood numbers with parameters shown in table I. The initial fluid interface is chosen to locate at $L_z/2$ for the low and middle Atwood cases, and at $2L_z/3$ for the high Atwood number case, to allow for the unequal development of bubble and spike at high $\mathcal{A}$. The perturbation Reynolds number is defined as $\mathrm{Re}_p = \lambda\sqrt{\mathcal{A}g\lambda/(1+\mathcal{A})}/\nu$, and the mesh Grashof number is $\mathrm{Gr} = 2\mathcal{A}g\Delta x^3/\nu^2$, whose value below 1 indicates that the simulation is well resolved [16]. The $\mathrm{Gr} > 1$ for the middle and high Atwood number cases indicates that the simulation might be under resolved at very late time when chaotic structures emerge [17], which has not been reached in our middle and high $\mathcal{A}$ simulations as will be shown below. The $\mathcal{A} - \mathrm{Re}_p$ combination in 2DlowAt is to ensure that the bubble and spike would enter the reacceleration stage, according to the prediction by the phase diagram in reference [17]. The kinematic viscosity $\nu = \mu/\rho_I$ is the ratio of dynamic viscosity and interficial density defined as $\rho_I = (\rho_h + \rho_l)/2$ [17], and the Prandtl number $\mathrm{Pr} = \mu c_p/\kappa$ as well as the Schmidt number $\mathrm{Sc} = \nu/D$ are both unity, where c_p is the specific heat at constant pressure. Note that in the current paper, the main focus is on the morphology and dynamics of the low Atwood number RT, while the middle and high $\mathcal{A}$ cases are included for reference purposes only.

III. VISUALIZATION AND MIXING WIDTH GROWTH

Figure 1 presents the density field snapshots of the three RT cases at different time instants, together with selected tracer particles located at the bubble, the spike, and the spiral regions. The spiral region denotes the primary vortical structure formed by baroclinicity $1/\rho^2(\nabla\rho\times\nabla P)$, which arises from the misalignment between the density and pressure gradi-

TABLE I. Parameters of the 2D single-mode RT simulations. L_x and L_z are the domain widths along the horizontal and vertical directions, respectively. The Mach number $\mathcal{M}$ is measured as a maximum value among all snapshots of the corresponding simulation.

	Grids	L_x	L_z	$\mathcal{A}$	μ	Re_p	Gr	$\mathcal{M}$	Pr	Sc
2DlowAt	512×2048	0.4	1.6	0.15	1.2×10^{-5}	6621	0.75	0.08	1	1
2DmidAt	512×2048	0.4	1.6	0.5	1.2×10^{-5}	8114	1.47	0.11	1	1
2DhighAt	512×2048	0.4	1.6	0.8	1.2×10^{-5}	7808	1.63	0.15	1	1

ents near the fluid interface. We select these particles at the time instant in which the spiral is well developed (at non-dimensional time $\widehat{t} = t\sqrt{\mathcal{A}g/\lambda} = 2.94$), and then perform particle tracking both backward and forward in time to obtain their full evolution trajectories. For the low $\mathcal{A}$ simulation, the three sets of particles cover most of the interfacial regions at late time as shown in figure 1 (c) and (d). The total number of particles associated with the bubble, the spike, and the spiral regions are 2772, 2670, and 5829, respectively. Similar results also hold for middle and high $\mathcal{A}$ cases in panels (e),(f) and (g),(h), respectively, except that with increasing Atwood number, the fluid interface growth rate is increased and the selected particles fail to cover all the fluid interface. The total number of bubble, spike, and spiral particles are 2045, 1856, 4004 for the $\mathcal{A} = 0.5$ case and 1880, 1738, 2360 for the $\mathcal{A} = 0.8$ case.

The single-mode bubble and spike growth rate is one of the most important quantities for practical applications of RT [3]. To verify our numerical simulations and to introduce the different characteristic evolution stages in single-mode RT, here we show in figure 2 the Froude number of the bubble and the spike tip, $\mathrm{Fr}_{B/S} \equiv U_{B/S}/\sqrt{\frac{A}{1\pm A}g\lambda}$, which represents the non-dimensional velocity. For the low $\mathcal{A}$ case in figure 2(a), both the bubble and spike experience an initial exponential growth, and then follow by a saturation at Froude number $\mathrm{Fr} = \sqrt{\frac{1}{3\pi}}$, as is predicted by the potential flow theory [23]. After the nonlinear saturation, both the bubble and spike start to reaccelerate and their velocities keep growing. According to Wei and Livescu [16], the system would eventually enter the chaotic mixing stage with constant mean acceleration in the bubble and spike tips. However, our current simulation domain is not long enough to allow for such a stage. In figure 2 (a), we highlight different stages in the figure, namely the exponential growth stage (EG), the nonlinear saturation

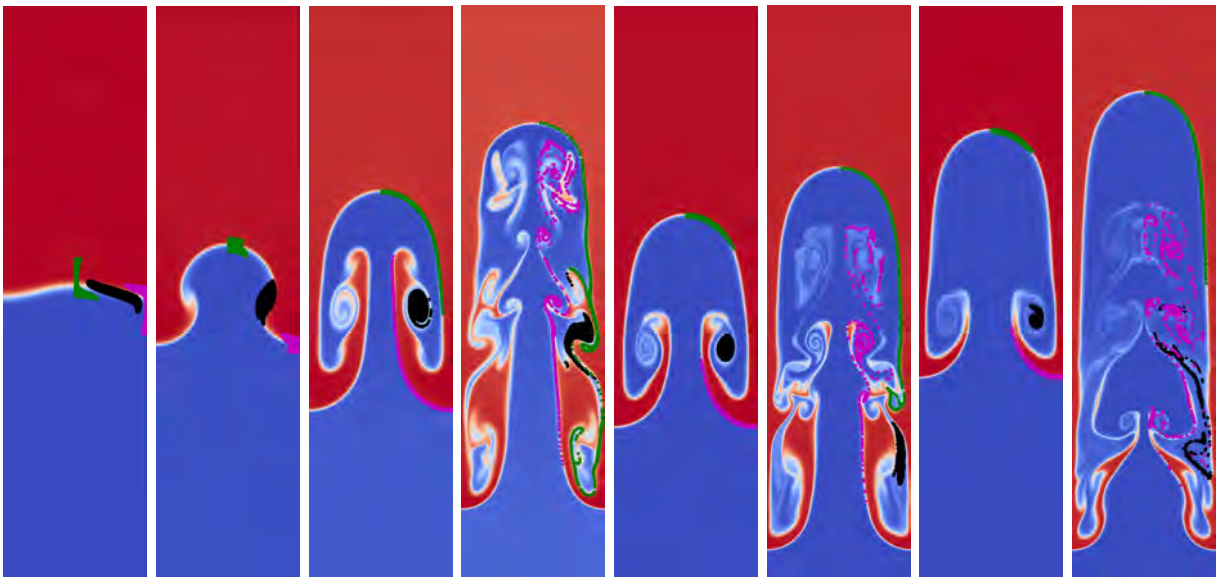

(a) (b) (c) (d) (e) (f) (g) (h)

FIG. 1. The visualization of the density fields at non-dimensional time $\widehat{t} = t\sqrt{\mathcal{A}g/\lambda} = 1.22$, 2.45, 3.67, 4.90 for 2DlowAt in panels (a)-(d), and at $\widehat{t} = 3.67$, 4.90 for 2DmidAt in (e),(f) and for 2DhighAt in (g),(h), respectively. In each panel, we show 1/100 of all selected particles in green (·), black (·), and magenta (·) to mark particles at the bubble, the spiral, and the spike regions. In the Supplementary Materials, we have included movies illustrating the temporal evolution of these selected particles imposed on the density fields for a better visualization.

or the potential flow growth stage (PFG), and the re-acceleration stage (RA). This temporal partition into three stages allows us to perform conditional Lagrangian tracer particle statistics, as will be illustrated below. Note that we have neglected the early part of the exponential growth (EG) stage in our statistics (the EG stage does not start near the origin), since during this period the tracer particles are nearly quiescent and the statistics would be trivial.

For the middle and high Atwood number cases in figures 2(b) and (c), the bubble velocity saturates after exponential growth, with a terminal velocity close to the theoretical prediction, but the saturation velocity persists till late time and no reacceleration occurs. This behavior is compatible with the $\mathcal{A}$-Re$_p$ phase diagram proposed by Bian et al. [17]. Growth of the spike velocity is more complicated. For $\mathcal{A} = 0.5$ in panel (b), the spike reaccelerates after a short plateau with a velocity slightly higher than the theoretical prediction, while for $\mathcal{A} = 0.8$, no plateau is observed and the spike velocity keeps increasing. The spike behavior

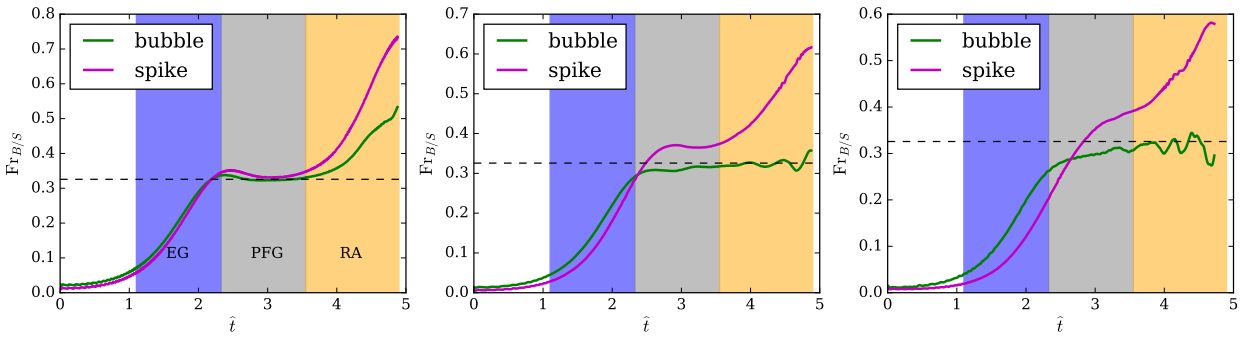

(a) $\mathcal{A} = 0.15$ (b) $\mathcal{A} = 0.5$ (c) $\mathcal{A} = 0.8$

FIG. 2. The velocity at the bubble and spike tips for (a) low, (b) middle, and (c) high Atwood number RT simulations. In each panel, the horizontal dashed lines represent theoretical predictions [23], $\mathrm{Fr}_{B/S} = \sqrt{1/3\pi}$ for all cases. In panel (a), three stages denoted EG, PFG, and RA are highlighted.

has also been observed in reference [17], in which the high spike velocity is attributed to the thin vortical structures emerging from the spike tip at relatively high $\mathcal{A}$.

In the following sections, we will investigate the statistics of Lagrangian tracer particles near the fluid interface, focusing on the low $\mathcal{A}$ case in which the bubble-spike structure is more symmetric and the Kelvin-Helmholtz instability is well developed, while the middle and high $\mathcal{A}$ results are included for reference. The statistics is performed on the three ensembles of tracer particles in the bubble, the spike, and the spiral regions, which we shall call the bubble/spike/spiral particles, and also within each of the three temporal stages marked as EG, PFG, and RA. We will first study the geometrical properties of particle trajectories, and then investigate their influences on the dynamical evolution of fluid interfaces. Anisotropy associated with the kinetic energy of the fluid interface will also be analyzed via the Lagrangian approach. Here, we focus on vector anisotropy, which is different from the shape anisotropy of RT flows studied recently in [51].

IV. GEOMETRY OF PARTICLE TRAJECTORIES

As have shown in figure 1, three ensembles of Lagrangian tracer particles associated with the bubble, the spike and the spiral regions are chosen for Lagrangian investigation. The trajectories associated with the three groups of particles are illustrated in the three panels of figure 3, in which visual similarity of the trajectories is shared among each group. For

example, in panel (a) the bubble particles emerge from the middle of the domain and initially move upwards, and then their trajectories start to bend and gradually move downwards. Finally the bubble particle trajectories are more complex, and some of which are subjected to swirling motions. The movement of the spike particles in panel (b) is almost opposite to the bubble particles, since at low $\mathcal{A}$ the bubble and spike structures are close to symmetric. Meanwhile, spiral particles are driven mainly by vortical flows and undergo swirling motions during their lifetime, as is evident in the trajectories shown in panel (c). For middle and high $\mathcal{A}$ cases, the particle trajectories are qualitatively similar to their low $\mathcal{A}$ counterpart, but the center of the spiral particles gradually shifts downwards in addition to the swirling motion, due to the asymmetric movement of the heavy and the light fluids in the presence of large density contrast.

Given the distinct characteristics of particle trajectories, the statistics associated with each of the three ensembles would be different. Figure 4 shows the probability density function (PDF) of trajectory curvature κ associated with different particle ensembles at various stages. The curvature is defined as $\kappa = (z''x' - x''z')/|x'^2 + z'^2|^{3/2} = (-u_z a_x + a_z u_x)/|u|^3$, where $x(t)$ and $z(t)$ are particle coordinates parameterized by time, the prime symbol $'$ denotes time derivative, and a is the particle acceleration. The trajectory curvature (together with the torsion) fully determines any space trajectory, and it is related to small scale dynamical quantities such as acceleration, vorticity, and dissipation [52]. We show the correlation between particle trajectory curvature and particle acceleration in Appendix C. Overall, curvature associated with the spiral particles is higher than the bubble and spike particles, as can be determined from visual inspection of the respective trajectories in figure 3. The curvature magnitude of the bubble and spike particles gradually increases in time, and in the RA stage their magnitude is comparable to the spiral particles as indicated in figure 4 (c).

In addition, in figure 4(a)-(c) the PDFs of spiral particle trajectories scale as κ^{-3} at the right κ tail during all the three stages. This scaling of the spiral particles can be well explained by geometrical arguments. The spiral is approximately a uniform circular region of radius R, and the probability density of radius r inside this circle is $P(r)dr = 2\pi r dr/(\pi R^2)$, or $P(r) \propto r$. The curvature κ, which is the inverse of the radius of curvature, is another random variable which roughly satisfies $\kappa \sim r^{-1}$. By the change of variable formula of the PDF, we get $P(\kappa) \propto \kappa^{-3}$, same as the scaling in figure 4. The scalings of bubble and

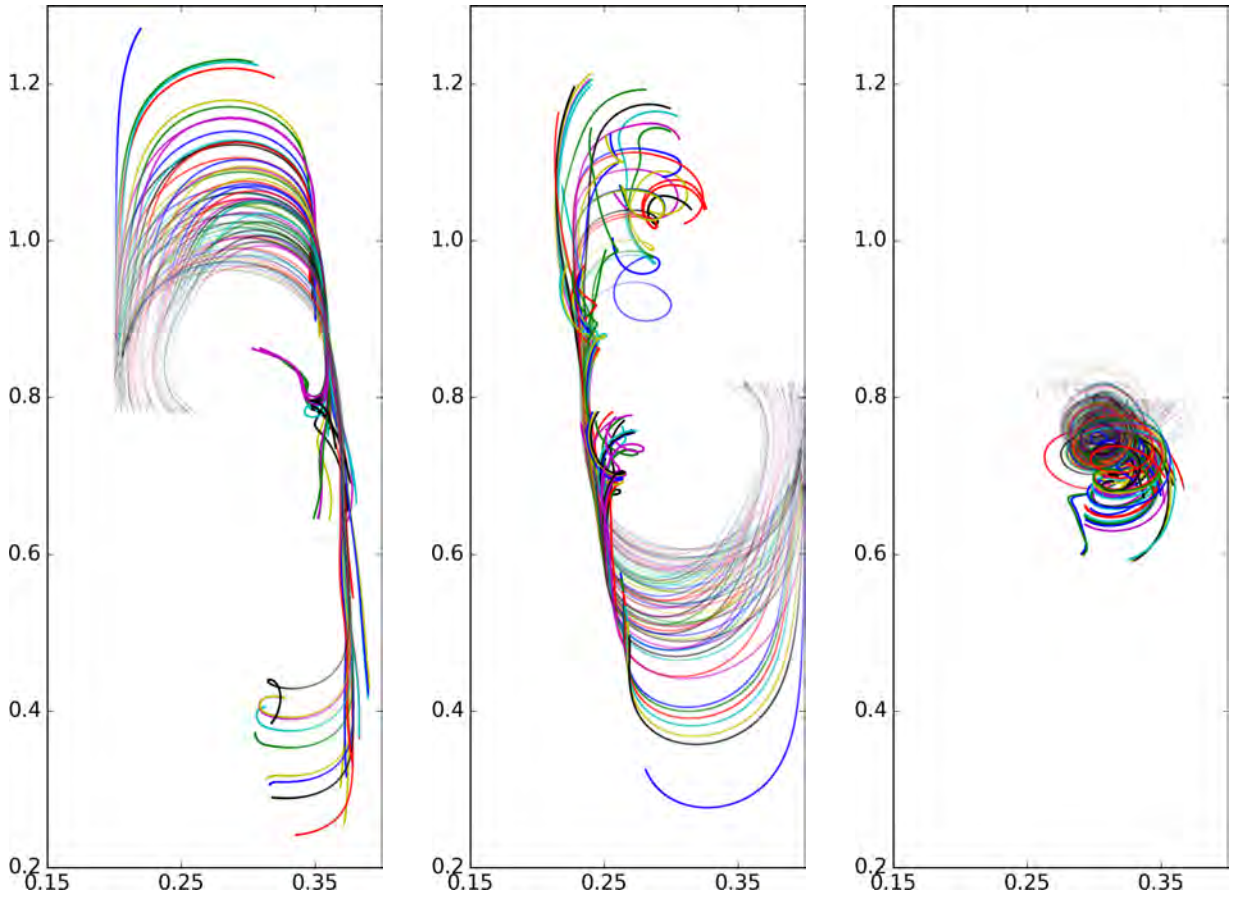

(a) bubble (b) spike (c) spiral

FIG. 3. The trajectories of particles associated with the bubble (a), the spike (b), and the spiral (c) regions within non-dimensional time $0 < \widehat{t} < 4.9$. The domain is truncated to lie within $0.15 < x < 0.4,\ 0.2 < z < 1.3$ for a better presentation, and only 1/100 of the particles in each ensemble is shown here. To emphasize the time variable, the transparency of each trajectory varies continuously from transparent colors at the initial time instant to solid colors at the final time instant.

spike particle trajectories in the EG and PFG stages decay rapidly at the high κ end, while in the RA stage, their scalings are around κ^{-2}, corresponding to a uniform distribution of the radius of curvature. This is a reasonable result, considering that in the RA stage the bubble and spike particles are scattered in space and hence are weakly correlated among their respective ensemble, such that the distribution of the radius of curvature is roughly uniform. Gaussian statistics.

The PDF of normalized particle speed $\widehat{u} \equiv |\mathbf{u}|/\sqrt{\mathcal{A}gL_x}$ is shown in figure 4 (d)-(f), with a

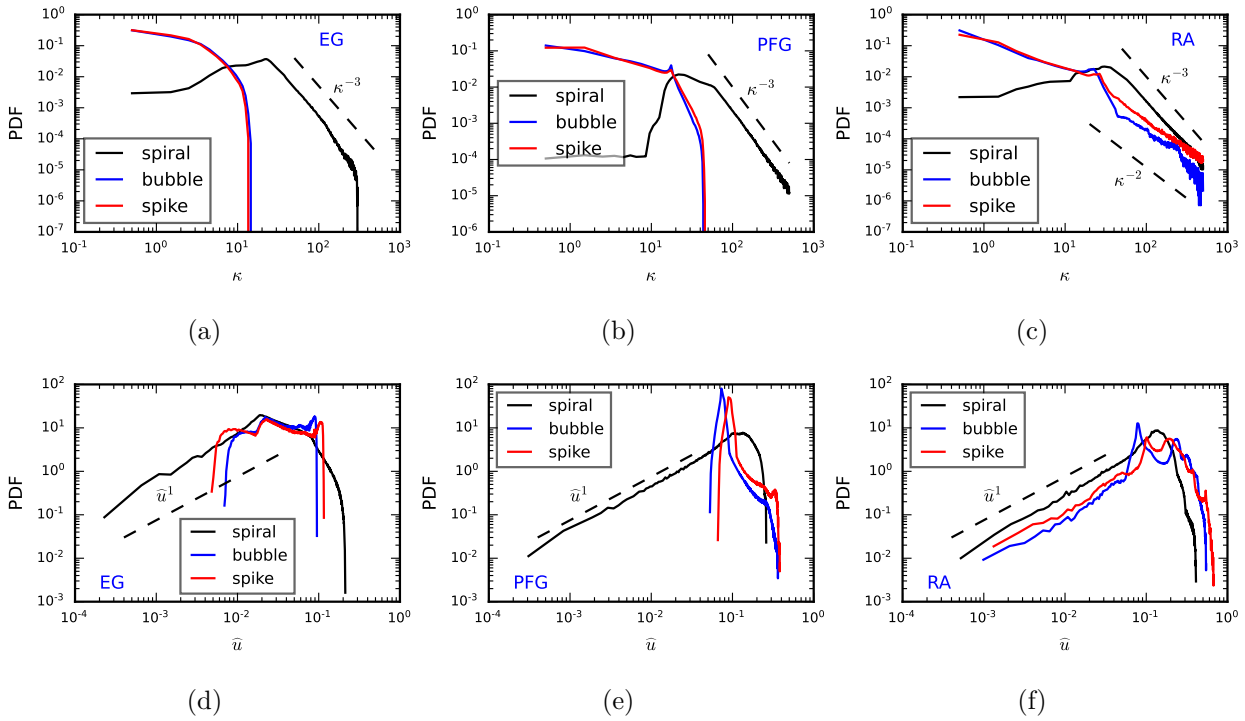

FIG. 4. The probability density functions (PDFs) of the trajectory curvature associated with the bubble, spike, and spiral particles. Panels (a),(b), and (c) show the results during the EG, PFG, and RA stages, respectively. A dashed line with a -3 slope is included in (a)-(c) for reference. Panels (d)-(f) show the PDFs of normalized particle speed $\widehat{u} = |\mathbf{u}|/\sqrt{\mathcal{A}gL_x}$ in the three stages, and a dashed line with slope 1 is included for reference.

reference line $\widehat{u}^1$ included in each panel. The speed of spiral particles exhibits a $\widehat{u}^1$ scaling in the left tail of the PDFs during all the three stages, because the spiral particles are co-moving along circular trajectories with $|\mathbf{u}| = \Omega_u r$ (Ω_u is the angular velocity of the spiral particles), since $P(r) \sim r^1$ we have $P(\widehat{u}) \sim \widehat{u}^1$. For the bubble and spike particles in the EG and PFG stages, no clear scaling is visible, and their minimum speed is relatively large compared to spiral particles due to the large-scale convective motion. However, it is interesting to note that in the RA stage the $\widehat{u}^1$ scaling of both the bubble and spike particles is realized, with comparable PDFs for all the three particle ensembles.

More detailed information relating particle curvature κ and speed $\widehat{u}$ is contained in the joint PDFs shown in figure 5. For spiral particles in the EG stage of panel (a), at small values κ increases with $\widehat{u}$, while at large values κ decreases with increasing $\widehat{u}$. In the PFG and RA stages, the curvature of spiral particles decrease with increasing speed, consistent with the relation $\kappa \sim 1/r$ and $u \sim \Omega_R r$. The results for the bubble particles are included

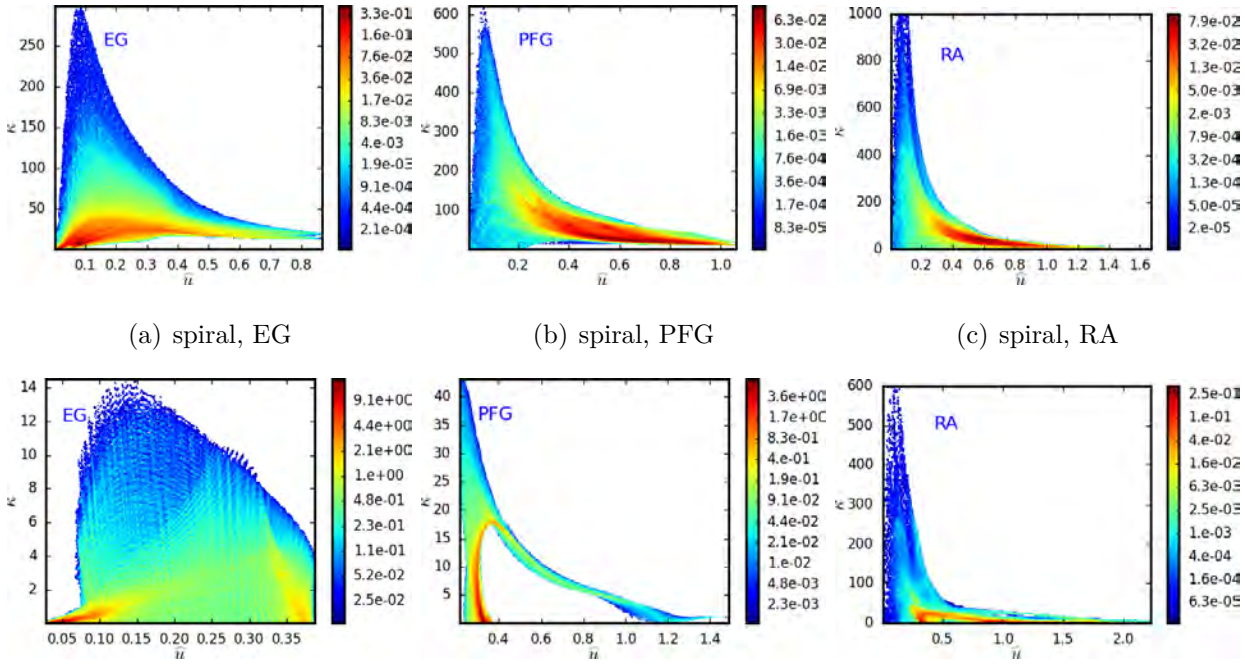

(a) spiral, EG (b) spiral, PFG (c) spiral, RA

(d) bubble, EG (e) bubble, PFG (f) bubble, RA

FIG. 5. The joint PDFs of trajectory curvature κ with normalized speed $\widehat{u}$ of the spiral particles at different stages in panels (a)-(c), and of the bubble particles in panels (d)-(f).

in panels (d)-(f). During the EG stage of panel (d), the bubble particle trajectories are close to straight lines, thus its curvature is much smaller compared to the spiral particles at the same stage, with no clear trend exists between κ and $\widehat{u}$. In the PFG stage, the curvature is still much smaller than the spiral, but the joint PDF exhibits two branches. The left branch ($\widehat{u} < 0.4$) is associated with slow particles, whose trajectory curvature spans a wide range but is almost invariant with respect to $\widehat{u}$; while in the right branch κ decreases with increasing $\widehat{u}$, consistent with the fact that some of the bubble particles are subjected to large-scale swirling motion. Finally, in the RA stage, the bubble particle curvature is comparable to the spiral particle, and the joint PDF is also similar, which is due to more swirling bubble particles at the late stage. The results of the spike particles are very similar to the bubble particles, and in addition similar joint PDFs exist for the middle and high $\mathcal{A}$ cases.

The different trajectories of the bubble, spike, and spiral particles will exert different influences on the topological evolution of the fluid interface and on general RT dynamics such as the bubble reacceleration. We will consider these influences in the next section.

V. LAGRANGIAN DYNAMICS OF THE FLUID INTERFACE

A. Growth of the fluid interface

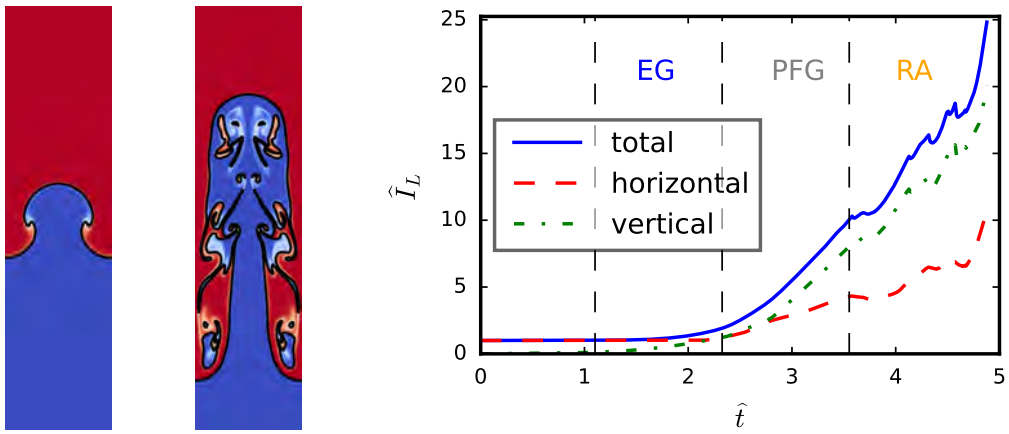

(a) (b) (c)

FIG. 6. Panels (a) and (b) show the contour line $Y_1 = 0.5$ imposed on the background field of Y_1 at non-dimensional time $\widehat{t}$=2.45 and 4.90. Panel (c) shows the total length of the 2D contour line $Y_1 = 0.5$ as a function of time, together with the lengths of its horizontal and vertical projections. The interface length is normalized by L_x.

During RT development, the heavy-light fluid interface is continuously deformed and stretched by the instability, which leads to the formation of fractals in the case of 2D multi-mode RT with a fractal dimension of 1.7-1.8 [53]. In our single-mode RT case, we will measure the total interfacial length and relate its temporal growth with the tangential strain carried by the particles associated with the bubble, spike, and spiral regions. Here the fluid interface is defined by the contour line $Y_1 = 0.5$ in the 2D field, which is shown as black lines in figure 6 (a), (b) at early and late times, respectively. Due to the effects of advection and diffusion, the contour line at late time is broken into several unconnected pieces, and the interface length is the sum of all the individual parts. Note that the topology of the interface contour is sensitive to the Reynolds number Re under study. Increasing Re could result in rich small-scale vortices induced by the Kelvin-Helmholtz instability, which adds fine details to the contours shown in panels (a) and (b) of figure 6. Thus it is desirable to resort to some quantitative measures such as the total length of the interface, whose qualitative evolution trend is not sensitive to Re, given that the RT flow undergoes all the three stages (the EG,

PFG, and RA stages) at the particular Re.

Figure 6 (c) shows temporal evolution of the total interface length $\widehat{I}_L$, together with the length projected onto the horizontal and vertical directions. During the EG stage, the total length as well as its horizontal and vertical projections are slowly increasing. In the RT initial condition the interface is horizontal and the vertical projection is zero initially, but the vertical component grows faster than horizontal, and exceeds the latter at the end of the EG stage. In the PFG stage, the total length increases rapidly, with the vertical component dominates over the horizontal. In the RA stage the increasing trend continues, and the vertical component is more than two times larger than the horizontal. Compared to the EG and PFG stages, there are wiggles appearing in the curves during the RA stage in figure 6 (c), which is attributed to the broken of contour line into several parts, and disappearance of small isolated islands of fluids due to the excessive diffusion exerted on the long, thin structures emerged from the spike tip, as is illustrated in figure 6 (b). The middle and high $\mathcal{A}$ results are qualitatively similar to figure 6, but the total interface length increases with Atwood number, since the potential-to-kinetic energy conversion is more efficient and the instability grows faster when the Atwood number is higher, as is indicated by the dimensional bubble and spike velocities $U_{B/S} = Fr_{B/S}\sqrt{\frac{\mathcal{A}}{1+\mathcal{A}}g\lambda}$ of the three $\mathcal{A}$ cases as can be inferred from figure 2.

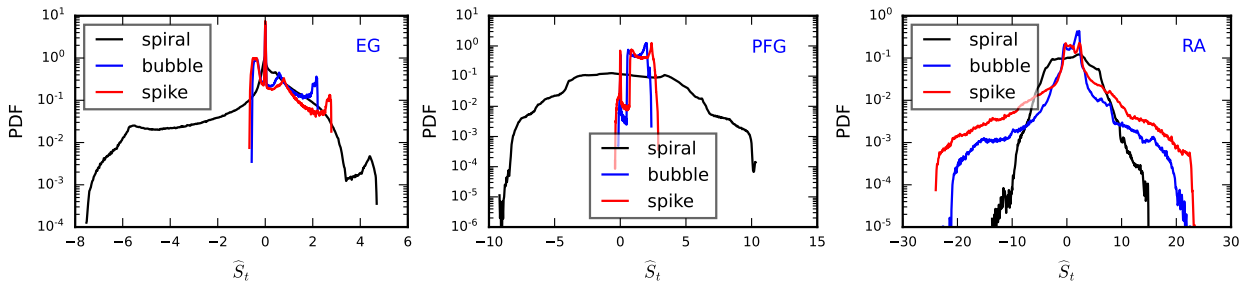

(a) (b) (c)

FIG. 7. The PDFs of tangential strain rate $\widehat{S}_t$ experienced by particles at different stages in panels (a)-(c), which is normalized by the reference time $\sqrt{\lambda/\mathcal{A}g}$. The mean values of $\widehat{S}_t$ associated with the spiral, bubble, and spike particles in panel (a) are -0.058, 0.36, 0.227, in (b) 0.228, 1.382, 1.626, and in (c) 0.788, 1.075, 0.920.

We further adopt the tangential strain rate S_t to characterize the local evolution of fluid interface. The tangential strain rate measures the stretching or compression along the

tangential direction of the interface and is defined as $S_t = (\delta_{ij} - n_i n_j)\frac{\partial u_i}{\partial x_j}$, where δ_{ij} is the Kronecker delta and $n_i = \frac{\partial Y_1}{\partial x_i}/|\frac{\partial Y_1}{\partial x_i}|$ represents the interface normal. The tangential strain rate constitutes a major component of the stretching K of the interfacial area $A \propto |\nabla Y|$ that

$$K = \frac{1}{A}\frac{dA}{dt}$$

which is related to the tangential strain rate S_t by

$$K = -n_i n_j \partial_i u_j + \partial_i u_i + S_d\ \partial_i n_i \equiv S_t + S_d\ \partial_i n_i \tag{5}$$

where $S_d = \frac{1}{|\nabla Y|}\frac{DY}{Dt}$ is the interface displacement speed [54].

Figure 7 shows the PDFs of normalized tangential strain rate carried by the spiral, bubble, and spike particles in the EG (a), PFG (b), and RA (c) stages. Qualitatively different behavior is observed between the spiral particles and the bubble/spike particles. During all three stages, both positive and negative S_t exist for spiral particles, indicating a simultaneous compression and stretching of the spiral interface at different locations; while for the bubble and spike particles, tangential strain rate is predominantly positive in the EG and PFG stages during which the interface expands, and in the RA stage the PDF of S_t is close to symmetric around 0, indicating that both compression and stretching of the interface are at work. Different patterns of tangential strain rate would lead to different topologies of bubble, spike, and spiral interfaces. For example, the ensemble-averaged tangential strain rate of the spiral particles is comparatively small in the EG and PFG stages and rises in the RA stage, thus the total length of the spiral is kept small during the initial period of RT evolution until a increase is observed in the late RA stage. The interface associated with bubble and spike, however, keeps increasing in all stages due to the relatively large mean $\langle S_t \rangle$, which is compatible with the visualization in figure 1 and the interface growth in figure 6.

We further illustrate an Eulerian visualization of S_t in figure 8 to complement the Lagrangian results. We observe in this figure that during the EG and PFG stages, the tangential strain rate S_t at the bubble and spike regions is positive, while S_t at the spiral region attains both positive and negative values with comparable magnitude. In the RA stage, the results are more chaotic and negative values emerge in regions where bubble and spike particles reside, in compatible with the PDFs shown in figure 7.

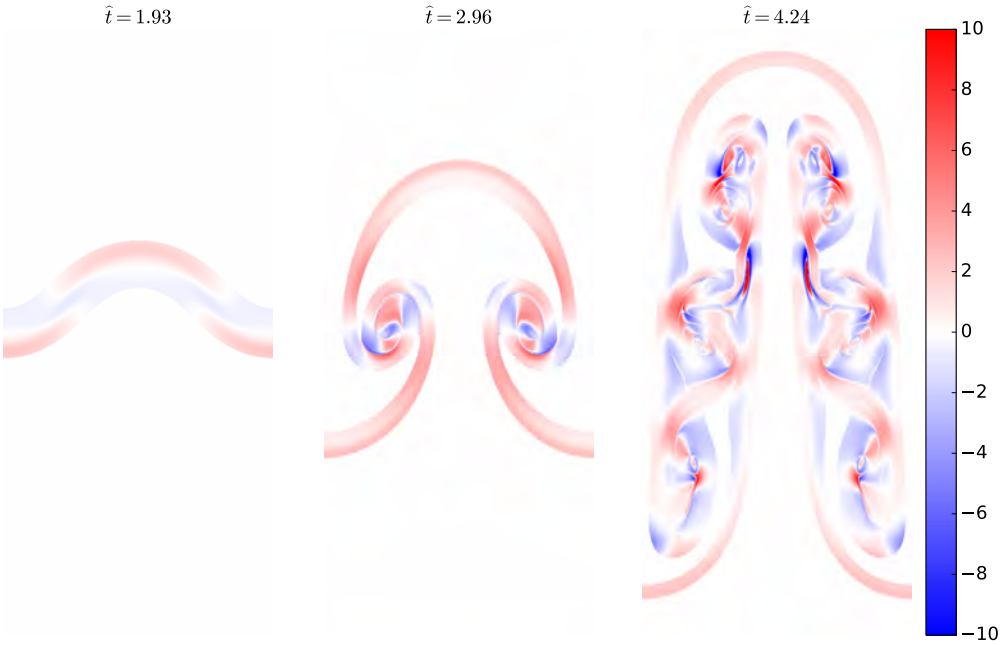

FIG. 8. Visualizations of the tangential strain rate S_t at three time instants $\widehat{t} = 1.93, 2.96, 4.24$ which belong to the EG, PFG, and RA stages, respectively. In all three panels we have truncated the vertical domain to show only the region $0.3 < z < 1.2$.

B. Secondary Rayleigh-Taylor instability in the spiral

During the nonlinear stages of RT evolution, spiral particles are subjected to centrifugal forces, which could potentially lead to the onset of secondary RT instability in local regions of the spiral [55]. This secondary RT could distort the spiral motion, render it unstable, and produce complex small-scale structures to enhance local turbulence development. An emblematic example of secondary RT is highlighted in the red boxes of figure 9, where additional 'arms' emerge from the spiral and influence its further development. We shall study the secondary RT instability based on the simple instability criterion $\nabla\rho\cdot\nabla P < 0$ resembling the baroclinic vorticity generation [56, 57] on spiral particles. From the momentum equation (3), the pressure gradient can be expressed as $\nabla P = \rho\boldsymbol{g} - \rho\boldsymbol{a}$ if we neglect the viscous contribution, where $\boldsymbol{a} = \frac{D\mathbf{u}}{Dt}$ is the acceleration field. Thus the above instability criterion reduces to $g\partial_z\rho + \boldsymbol{a}\cdot\nabla\rho > 0$, in which the first term $g\partial_z\rho$ denotes the contribution from the density stratification, which we shall call the buoyancy contribution; while the second term $\boldsymbol{a}\cdot\nabla\rho$ arises because of the local instantaneous acceleration and density gradient, which for spiral particles we shall denote the centrifugal contribution.

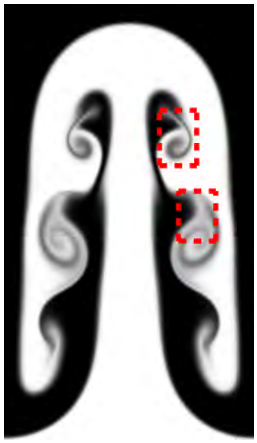

FIG. 9. The visualization of secondary RT instability near the spiral region at time $\widehat{t} = 4.10$. The grey background shows the visualization of the Y_1 field, and the two red rectangles denote the development of secondary instability.

The relative importance of the buoyancy and centrifugal contributions in the spiral region during the RT growth is shown in the joint PDFs in figure 10 for the three stages. The centrifugal contribution is close to symmetric in all stages, and its magnitude increases from the EG to the PFG stage, and then decreases over the RA stage. The buoyancy contribution is predominantly positive in the EG stage, and becomes more symmetric in the PFG and RA stages with comparable magnitude over the whole duration. The joint PDFs in both the PFG and RA stages in panels (b) and (c) is spontaneously split into two parts, depending on the sign of the centrifugal contribution. As we have mentioned, positive values of the sum of the centrifugal and buoyancy contributions indicate local RT unstable configuration, which we denote the secondary RT instability inside the spiral. Hence in figure 10(b) and (c), particles fall in the region above the dashed black line are RT unstable. Moreover, the centrifugal contribution in this unstable region is almost always positive, especially in the PFG stage. Thus we could argue that spiral particles with positive centrifugal contribution ($\boldsymbol{a} \cdot \nabla\rho > 0$) leads to the secondary RT instability with $\nabla\rho \cdot \nabla P < 0$.

Since the centrifugal contribution $\boldsymbol{a} \cdot \nabla\rho$ contains the acceleration field which is a Lagrangian quantity, it is desirable to find an Eulerian surrogate that can be calculated directly from only one snapshot. A possible candidate is the quantity $-\boldsymbol{\omega}\cdot(\nabla\rho\times\mathbf{u})$, whose joint PDF with the centrifugal contribution is shown in figure 11, where high correlation coefficients are observed. In other words, we have an approximation $\boldsymbol{a} \cdot \nabla\rho \approx -\boldsymbol{\omega} \cdot (\nabla\rho \times \mathbf{u})$ such that

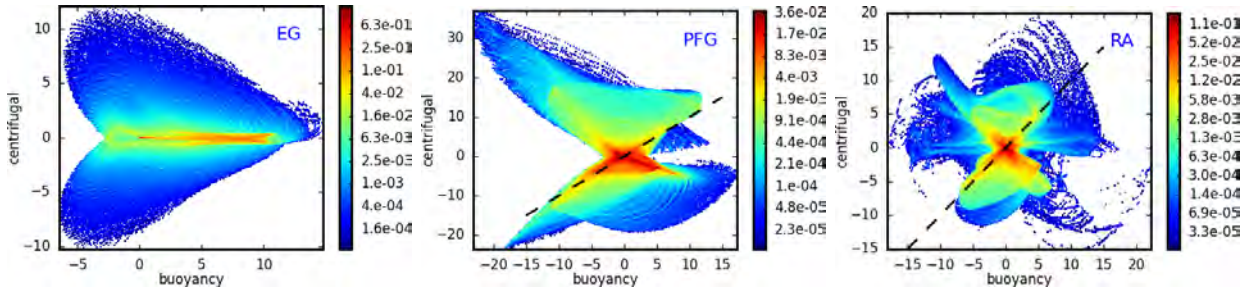

(a) (b) (c)

FIG. 10. The joint PDFs of buoyancy contribution ($g\partial_z\rho$) and centrifugal contribution ($\boldsymbol{a}\cdot\nabla\rho$) terms at the EG (a), PFG (b), and RA (c) stages associated with the spiral particles. In panels (b) and (c), the black dashed line represents the anti-diagonal line $y=-x$.

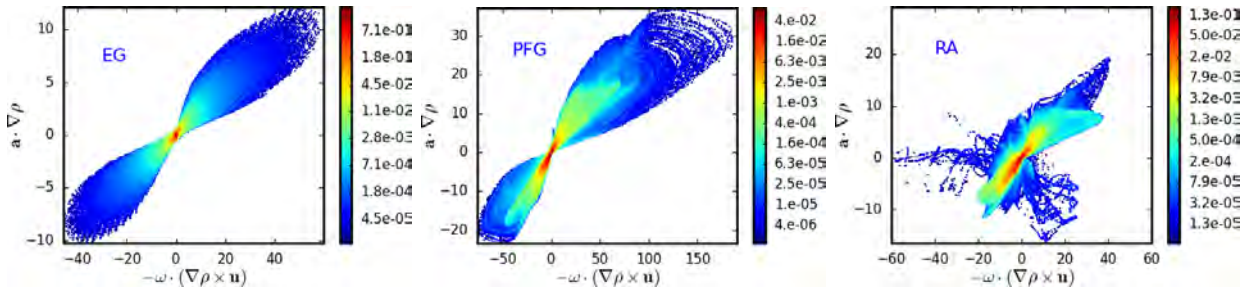

(a) (b) (c)

FIG. 11. The joint PDF of the centrifugal contribution ($\boldsymbol{a}\cdot\nabla\rho$) with the surrogate $-\omega\cdot(\nabla\rho\times\mathbf{u})$ in the EG (a), PFG (b), and RA (c) stages associated with the spiral particles. The correlation coefficient between the two quantities is 0.92 in panel (a), 0.93 in panel (b), and 0.85 in panel (c).

the criterion for the secondary RT instability inside the spiral $g\partial_z\rho+\mathbf{a}\cdot\nabla\rho>0$ can be recast as

$$g\partial_z\rho-\boldsymbol{\omega}\cdot(\nabla\rho\times\mathbf{u})>0 \tag{6}$$

The new criterion only depends on the instantaneous density and velocity fields, and is thus easier to evaluate than the original criterion.

The surrogate works because we have

$$\begin{aligned}-\boldsymbol{\omega}\cdot(\nabla\rho\times\mathbf{u})&=-\nabla\rho\cdot(\mathbf{u}\times\nabla\times\mathbf{u})=\nabla\rho\cdot(\mathbf{u}\cdot\nabla\mathbf{u}-\nabla\frac{|\mathbf{u}|^2}{2})\\&=\nabla\rho\cdot(\mathbf{a}-\frac{\partial}{\partial t}\mathbf{u}-\nabla\frac{|\mathbf{u}|^2}{2})\end{aligned} \tag{7}$$

which well approximates the centrifugal contribution $\boldsymbol{a}\cdot\nabla\rho$ for spiral particles, since these particles are restricted to a limited region and thus both the mean time derivative term

$\langle \frac{\partial}{\partial t}\mathbf{u} \rangle_{\text{spiral}}$ and the mean spatial transport term $\langle \nabla \frac{|\mathbf{u}|^2}{2} \rangle_{\text{spiral}}$ are small, where the average $\langle \cdot \rangle_{\text{spiral}}$ is over the spiral particle ensemble. From figure 11, during all the three stages in panels (a)-(c), the proposed surrogate is positively correlated with the centrifugal contribution with high correlation coefficients. For middle and high $\mathcal{A}$ cases, this surrogate term still applies, but with degraded correlation as $\mathcal{A}$ is increased. Also, the approximation is only valid for the spiral particles but not for the bubble and spike particles due to the above approximations.

C. Re-accelerations of the bubble and spike tips

Another application of interface Lagrangian tracking is to provide rationale for the re-acceleration of single-mode RT bubble and spike. The growth of bubble and spike velocity in figure 2(a) indicates that both the bubble and the spike tips reaccelerate in the RA stage. This phenomenon, particularly the bubble reacceleration, has been addressed in many previous studies [16, 17, 58, 59] due to its importance in predicting the bubble penetration depth, and is generally attributed to the influence of vortices generated near the spike and convected to the bubble tip. Reference [17] measured the vorticity averaged over a small region adjacent to the bubble tip, and found good correlation between the temporal evolution of the averaged vorticity and the bubble-tip velocity. Here we will measure the force acting on the bubble and spike tips, as well as the mean force on the nearby particles in the RA stage, to further corroborate the relation between bubble/spike re-acceleration and the convected fluids from the bubble or the spike regions.

Figure 12(a) shows, in the RA stage, the PDF of vertical force $f_z = \rho a_z$ experienced by the Lagrangian particles inside a rectangular domain enclosing either the bubble tip or the spike tip, with a vertical length L_x/π, similar to figure 13 of reference [17]. It should be noted that in the RA stage, particles near (below) the bubble tip are the upwards convected spike particles, and similarly, particles near (above) the spike tip are the downwards convected bubble particles, as is evident in the visualization of figure 1 (d). The PDF in figure 12(a) indicates that particles near the bubble tip are subjected to downward mean forcing over the RA stage, thus the particles will exert upward reaction force on the surrounding fluid and accelerate the bubble tip upwards. In the same way, the spike tip is subjected to downward forcing and also accelerate downwards in the RA stage. Panel (b) shows the temporal

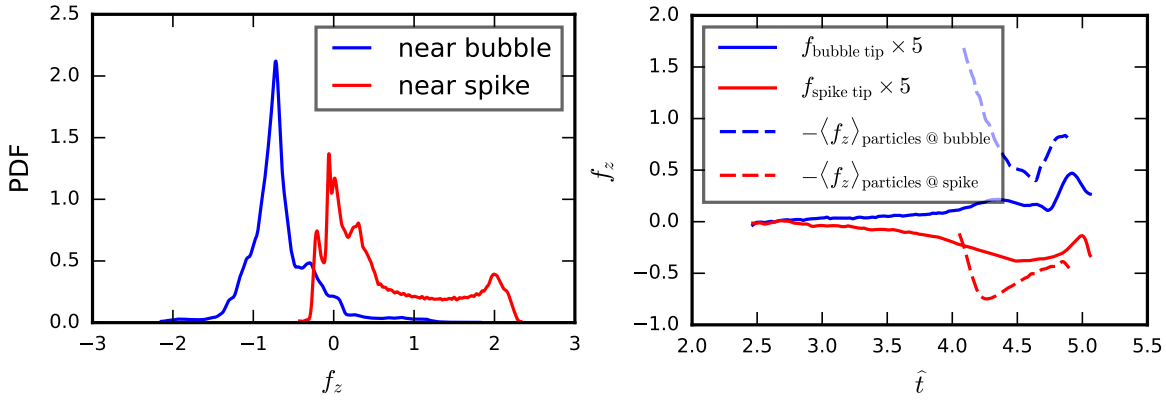

(a) (b)

FIG. 12. (a) PDFs of vertical forces on particles near the bubble and the spike tip during the RA stage, which are located within a rectangular domain with vertical length L_x/π as in reference [17], where f_z is the vertical force experienced by the Lagrangian particles. The mean values associated with particles near the bubble tip (blue) and near the spike tip (red) are -0.651 and 0.637. (b) Inside the same region, the instantaneous (vertical) forces on bubble and spike tips versus time, as well as mean vertical forces averaged over those selected particles. The dashed lines start around $\widehat{t} = 4.0$ when particles start to enter the enclosed region. The lines are re-scaled according to the descriptions in the legend.

evolution of the instantaneous forces measured on the bubble and the spike tips (multiplied by a factor of 5 for better comparison), which point along the vertical direction due to symmetry, as well as the mean forces exerted on the rectangle-enclosed particles (multiplied by -1 to denote the reaction forces from the particles to the surrounding fluids). The force history on the bubble tip is well correlated with the adjacent-particle mean reaction force, with a small time lag suggesting a possible causal relationship between the motion of particles near the bubble tip, which is convected from the spike side, and the bubble re-acceleration. The same situation also holds for the spike tip and the adjacent particles. Hence, figure 12 connects the bubble reacceleration to the convected fluids from the spike side using a Lagrangian point of view, complementing the Eulerian analysis proposed in reference [17].

VI. LARGE-SCALE VELOCITY ANISOTROPY NEAR THE INTERFACE

In this section, we study the evolution of velocity and kinetic energy (KE) of single-mode RT interface with the Lagrangian approach, focusing on the anisotropic development of interfacial KE along the horizontal and vertical directions. Understanding the anisotropic growth of fluid interface is conducive to characterizing the growth rate of RT bubble and spike in the nonlinear stage, and lays foundation for phenomenological models of RT. Figure 13 shows the PDFs of horizontal and vertical velocities associated with the spiral, bubble, and spike particles, ranging over the EG, PFG, and RA stages, which exhibit different statistical behavior as detailed in the follows.

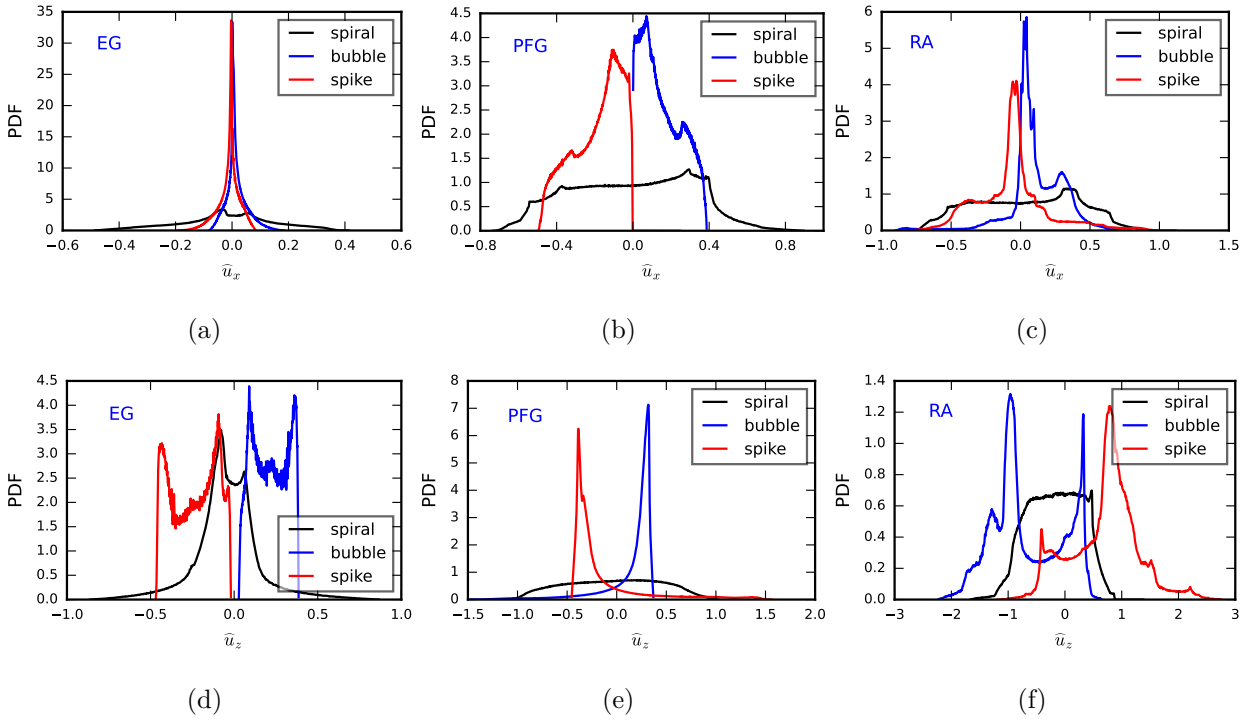

FIG. 13. The PDFs of the normalized horizontal velocity $\widehat{u}_x$ in panels (a)-(c), and of the normalized vertical velocity $\widehat{u}_z$ in panels (d)-(f) in the EG, PFG, and RA stages, respectively. Velocity is normalized by $\sqrt{\mathcal{A}gL_x}$.

In the EG stage, the PDF of horizontal velocity in figure 13 (a) is close to symmetric for all three particle ensembles, while for the vertical velocity, panel (d) shows that bubble particles only move upwards while the spike particles only move downwards, compatible with early RT flow patterns. In addition, the magnitude of $\widehat{u}_z$ is larger than that of $\widehat{u}_x$ within all three particle groups. These differences in the EG stage can be understood from

the streamline visualization in figure 14. The streamlines indicate that the bubble velocity is predominantly upwards and thus $\widehat{u}_z$ is positive for bubble particles, while (in the right half of the visualization) $\widehat{u}_x$ is negative in the lower part of the bubble interface and positive in the upper part, leading to a symmetric PDF around 0. The flow pattern near the spike tip is similar to the bubble tip except with the flow direction reversed. Meanwhile, the spiral particles lies around the middle of the swirling vortex in figure 14 and both the PDFs of $\widehat{u}_x$ and $\widehat{u}_z$ are symmetric.

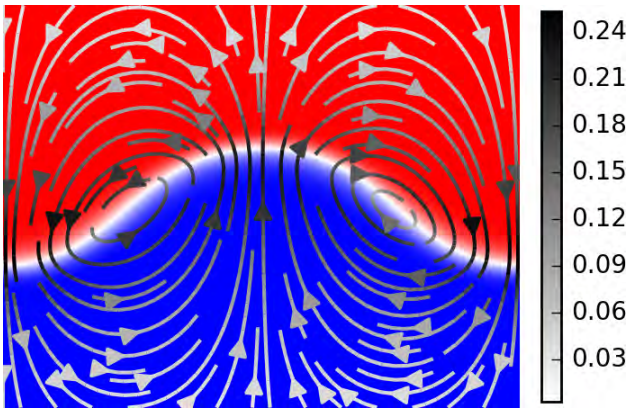

FIG. 14. The streamlines imposed on the density field of the low Atwood number RT within the EG stage, at non-dimensional time $\widehat{t} = 1.72$. The figure is truncated in the vertical direction for a clear presentation. The binary color-bar represents the velocity magnitude on streamlines.

In the PFG stage of figure 13 (b) and (e), both $\widehat{u}_x$ and $\widehat{u}_z$ are predominantly positive for the bubble particles, and are predominantly negative for the spike particles, while for the spiral particles the PDFs of $\widehat{u}_x$ and $\widehat{u}_z$ are close to symmetric. During this stage, the anisotropy between the horizontal and vertical velocities is apparent, with the magnitude of $\widehat{u}_z$ larger than $\widehat{u}_x$. As the system evolves from the PFG to the RA stage, velocity PDFs associated with the spiral particles are qualitatively unchanged, while for the bubble and spike velocity PDFs the changes are apparent. For $\widehat{u}_x$ in the RA stage, negative values appear within the bubble particles, and positive values appear within the spike particles, in contrast to the corresponding one-sided PDFs of $\widehat{u}_x$ during the PFG stage. More drastic change appears on $\widehat{u}_z$, whose PDF associated with the bubble particles shifts from positive-dominant in the PFG stage to negative-dominant in the RA stage, and vice versa for the spike particles. This occurs since the interface tangential velocity moves a large proportion of the bubble particles to the spike side, and spike particles to the bubble side, hence alters

the particle dynamics, as can be inferred from the particle locations in figure 1(c) and (d).

Given the dissimilar growth of horizontal and vertical velocities, we study quantitatively the directional anisotropy of kinetic energy, namely the ratio of horizontal to vertical KE. The anisotropy of RT is conducive to quantifying the distribution of energy among each direction, and influences the RT mixing width growth [13, 49]. Figure 15 (a) shows the temporal evolution of mean horizontal and vertical KE averaged over the whole domain, as well as over the fluid interface defined by the region $0.4 < Y_1 < 0.6$. Both the domain averaged horizontal and vertical KE increases with time, with an increasingly larger difference between the two quantities. The evolution of the interface averaged KE roughly follows a similar trend as the domain averaged result, but is not monotonically increasing in time due to the complex structures emerged in RT at late time. Both the horizontal and vertical interface-averaged KE plateau in the vicinity of the PFG-to-RA transition stage, but their ratio increases rapidly afterwards.

More detailed information of KE anisotropy is contained in the PDFs of the horizontal KE fraction, $\mathrm{KE}_x/\mathrm{KE}$, of fluid particles shown in figure 15 (b)-(d). As can be seen from the mean values of the spiral particle PDFs, the kinetic energy is almost evenly divided along the horizontal and vertical directions. But for the bubble and spike particles, the mean horizontal KE is much smaller than the vertical. For example, mean values of $\mathrm{KE}_x/\mathrm{KE}$ for bubble and spike particles are close to zero in the EG stage, and increases to around 0.3 in the PFG stage, which decrease again to about 0.2 in the RA stage. Compared to the near equipartition of KE in 2D multi-mode RT [49], single-mode RT leaves most of the energy to the vertical direction, and its mixing width growth is thus faster than the multi-mode case.

The physical mechanism of the KE anisotropy can be explained by the statistics of horizontal and vertical accelerations. Figure 16 shows the joint PDFs between $\widehat{a}_x$ and $\widehat{a}_z$, the horizontal and vertical acceleration fields normalized by the gravitational acceleration g, of the three particle ensembles at different stages. For spiral particles in panels (a)-(c), the joint PDFs of $\widehat{a}_x$ and $\widehat{a}_z$ are close to circular shapes centered at the origin, with the radius increasing from the EG to the PFG stage, and stays similar during the RA stage. These plots indicate an isotropic growth of horizontal and vertical velocities of the spiral particles, in accordance with the kinetic energy ratio in figure 15 (b)-(d). However, the joint PDFs of bubble particles in figure 16 (d)-(f) exhibit differences between $\widehat{a}_x$ and $\widehat{a}_z$, both in the magnitude and in the sign. The mean magnitude of $\widehat{a}_z$ associated with bubble particles is

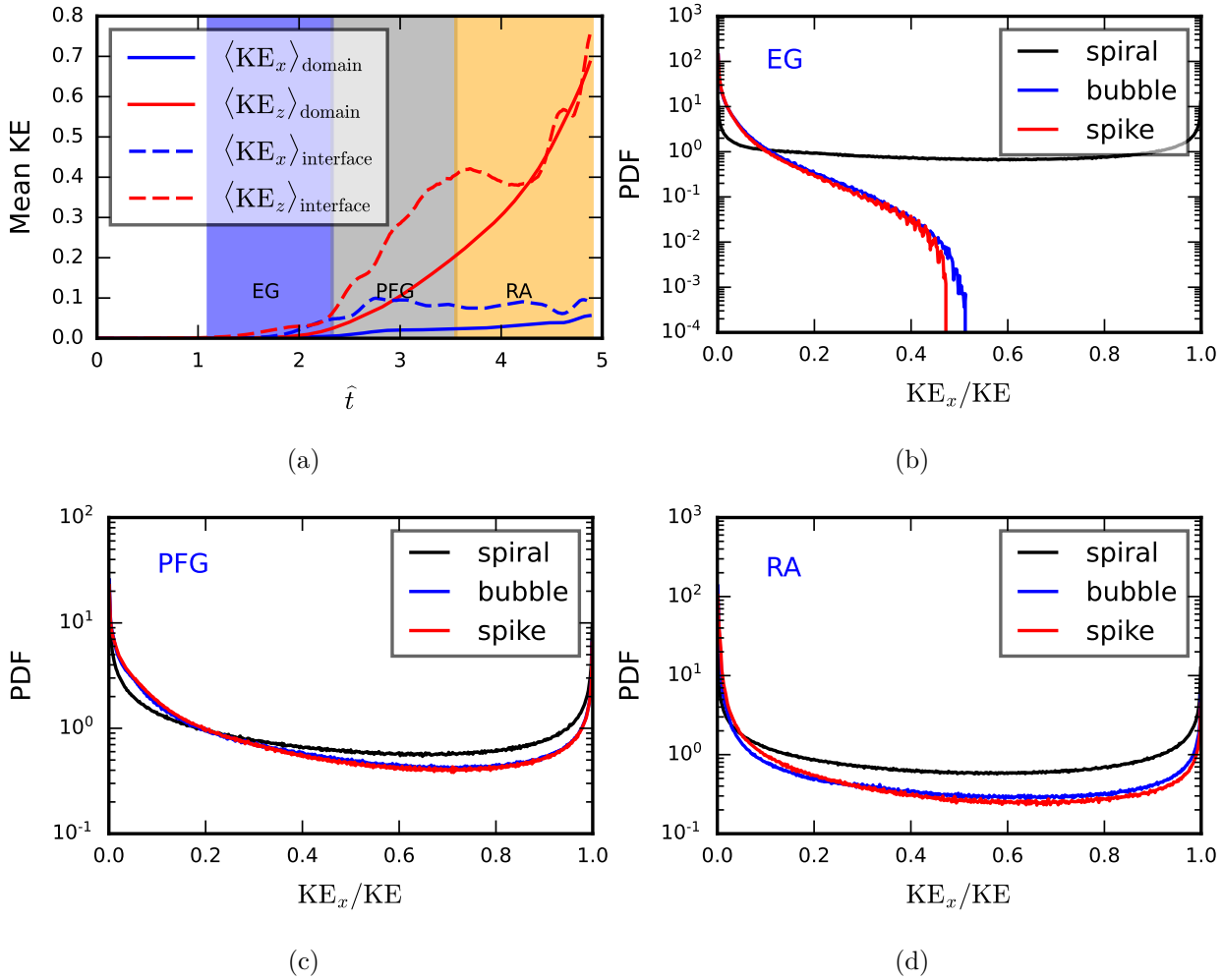

FIG. 15. (a): Time evolution of horizontal and vertical kinetic energy averaged over either the whole domain, or the fluid interface ($0.4 < Y_1 < 0.6$). The EG, PFG, and RA stages are highlighted. (b)-(d): The PDFs of the ratio of horizontal to total KE in the spiral, bubble, and spike regions, for each of the three stages. The mean values of the PDFs corresponding to spiral, bubble, and spike are 1): 0.488, 0.03, 0.03; 2): 0.408, 0.317, 0.310; 3): 0.452, 0.221, 0.194.

about 2-3 times larger than mean $\widehat{a}_x$. In addition, in the PFG and RA stages, $\widehat{a}_z$ is mostly negative, but $\widehat{a}_x$ attains both positive and negative values. In addition, u_z is predominantly negative in the two stages. Hence, $\widehat{a}_z$ continuously increases the magnitude of $\widehat{u}_z$, but the changing sign of $\widehat{a}_x$ leads to smaller magnitude of $\widehat{u}_x$. This phenomenon is related to the special configuration of single-mode RT, since along the horizontal direction the flow is confined by the lines of symmetry, while in the vertical direction no constraint is imposed except for the top and bottom walls which only affect RT development at very late time.

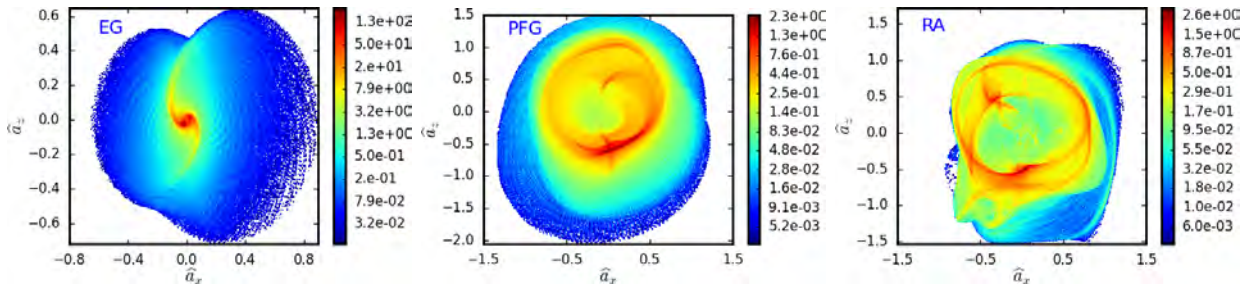

(a) spiral, EG (b) spiral, PFG (c) spiral, RA

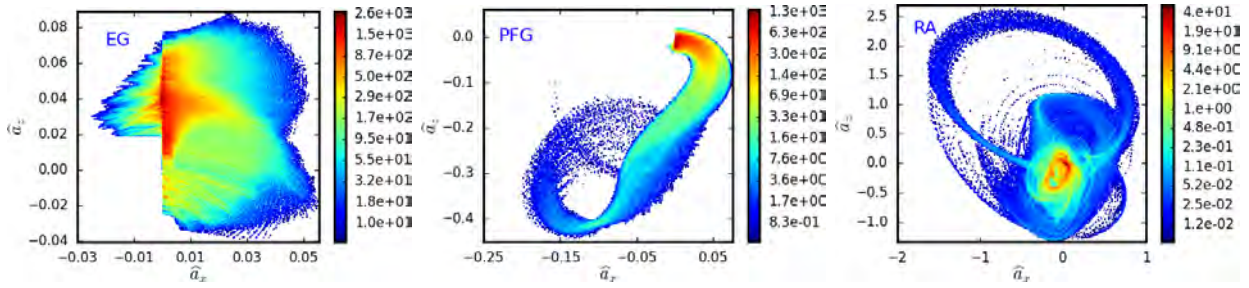

(d) bubble, EG (e) bubble, PFG (f) bubble, RA

FIG. 16. The joint PDFs of the horizontal and vertical acceleration associated with the spiral particles in panels (a)-(c) corresponding to the EG, PFG, and RA stages, and with the bubble particles in panels (d)-(f).

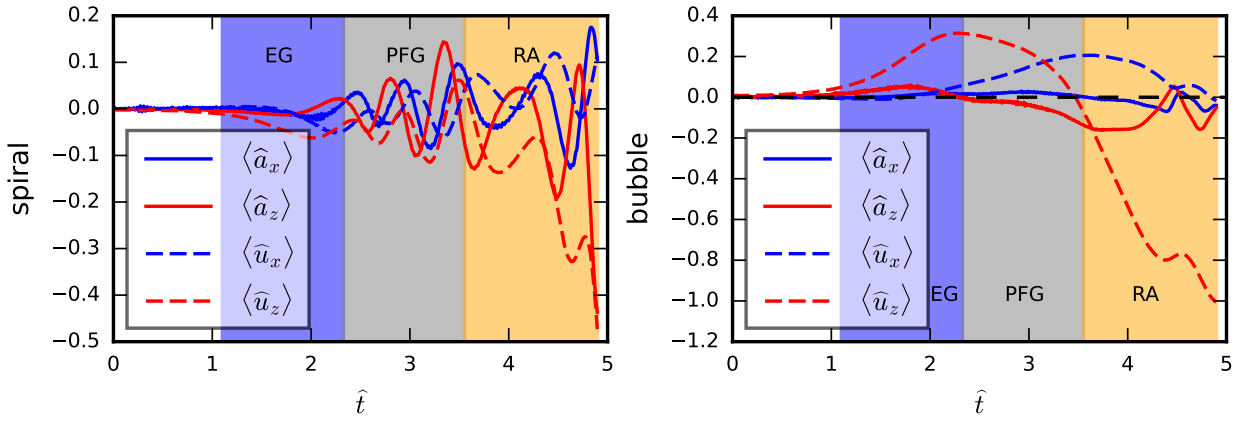

(a) spiral (b) bubble

FIG. 17. The mean values of non-dimensional velocity and acceleration versus time, averaged over the spiral particles in (a), and over the bubble particles in (b). The horizontal dashed black line in panel (b) corresponds to zero values. The non-dimensional velocity and acceleration are $\sqrt{\mathcal{A}gL_x}$ and g, respectively.

538 Figure 17 confirms the above argument by showing the temporal evolution of mean ac-

celeration and velocity averaged over the spiral and the bubble particle ensembles. In panel (a) for the spiral particles, both averaged $\langle \widehat{a}_x \rangle$ and $\langle \widehat{a}_z \rangle$ behave similarly, and $\langle \widehat{u}_x \rangle$ and $\langle \widehat{u}_z \rangle$ are comparable in magnitude. In contrast, for the bubble particles in panel (b), on one hand $\langle \widehat{a}_z \rangle$ is 2-3 times larger than $\langle \widehat{a}_x \rangle$ in magnitude; on the other hand $\langle \widehat{a}_x \rangle$ changes sign between the PFG and RA stages, while $\langle \widehat{a}_z \rangle$ is almost always negative during this period. Thus the averaged vertical velocity is much larger than the averaged horizontal velocity, in accordance with our previous analysis. Numerical tests also show that for the middle and high $\mathcal{A}$ cases, the KE anisotropy is similar to those low $\mathcal{A}$ results presented above.

VII. DISCUSSIONS AND CONCLUSIONS

This paper investigates the single-mode Rayleigh-Taylor instability with a Lagrangian approach, focusing on the topology and dynamics of the interface. Three particle ensembles are collected, including particles which pass through the bubble, the spike, and the spiral regions, to perform Lagrangian statistical analysis over different RT stages. A total of three stages, namely the exponential growth stage (EG), the potential flow growth stage (PFG), and the re-acceleration stage (RA), are identified based on the characteristics of RT flows, following the definition in reference [16]. The Lagrangian statistics studied in this paper including both kinematics associated with particle trajectories and the ensuing interfacial dynamics, which influences the topology of the interface, leads to secondary RT instability in the spiral, and accelerates the bubble and spike tips. The interface evolution also generates anisotropy between the horizontal and vertical kinetic energy components.

For the geometry of Lagrangian trajectories, we show that a κ^{-3} scaling appears in the right tail of the curvature PDF associated with the spiral particles during all stages, and for the bubble and spike particles at the RA stage the scaling is κ^{-2} due to a uniform distribution of the radius of curvature of particles. Fluid particles are trapped inside the vorticity-dominated spiral with high trajectory curvature compared to the shear-dominated bubble/spike particles undergoing large-scale convective motions. The joint PDFs between curvature and particle speed are more coherent with negative correlations for the spiral particles during all three stages, while for the bubble and spike particles the correlation is more complicated due to the relatively large dispersion within each of the particle ensembles.

The expansion of fluid interface is closely related to the tangential strain rate on the inter-

face. The PDF of tangential strain rate S_t indicates that for the bubble and spike particles, the net effect of S_t is to stretch the corresponding interface during all the evolution stages. In contrast, the spiral region tends to be compressed in the EG stage, and stretched in the PFG and RA stages. We then investigate the secondary RT instability inside the spiral region through the joint PDF of the buoyancy contribution ($-\boldsymbol{g} \cdot \nabla\rho$) and the centrifugal contribution ($\boldsymbol{a} \cdot \nabla\rho$) terms, and have found that positive centrifugal contribution is associated with the secondary RT instability. A surrogate term $-\omega \cdot (\nabla\rho \times \mathbf{u})$ for the centrifugal contribution in the spiral region is proposed, which depends only on the instantaneous Eulerian field instead of the Lagrangian time derivative. Finally, the re-acceleration of bubble and spike tips are shown to be correlated with the forcing exerted by Lagrangian particles transported to the adjacent regions in the RA stage, complementing existing Eulerian results in the literature.

The interface kinetic energy along x- and z-directions in single-mode RT exhibits distinct statistics in different regions, as measured by the ratio between the horizontal and the total kinetic energy. Associated with the spiral particles the flow is close to isotropy, while for the bubble/spike particles the KE anisotropy is pronounced and the horizontal velocity magnitude is much smaller compared to the vertical. This anisotropy is well explained by the joint PDFs between the horizontal and vertical accelerations. For bubble/spike particles, the ensemble-mean horizontal acceleration $\langle a_x \rangle(t)$ is smaller in magnitude compared to the vertical acceleration $\langle a_z \rangle(t)$, and in addition $\langle a_x \rangle(t)$ alters sign between the PFG and RA stages leading to a cancellation effect on $\langle u_x \rangle(t)$, thus giving rise to a much smaller horizontal KE than the vertical. The pronounced anisotropy effects should be taken into account in reduced numerical models such as Reynolds-averaged Navier–Stokes (RANS) or Large Eddy Simulations (LES).

To conclude, we adopt the Lagrangian approach to study the interfacial kinematics and dynamics of 2D single-mode RT instability. The ensemble of spiral particles undergoes approximately a solid-body rotation and the PDFs of its trajectory curvature and particle speed follow κ^{-3} and u^1 scalings, respectively, during all three evolution stages. In addition, the bubble and spike particles in the RA stage undergo spiral motions with uniformly distribution radius of curvature, and the κ^{-2} and u^1 scalings are observed. Lagrangian investigation of interfacial dynamics indicates that the interface near the bubble and the spike are continuously stretched, and the bubble/spike tip reacceleration is induced by the convected

vortices inside the adjacent regions; while for the spiral structure, both interface streching and compression exists, and the centrifugal acceleration inside the spiral induces a secondary RT instability which can distort its motion. Finally, we find that the anisotropy in interfacial KE is more pronounced for bubble and spike regions compared to the spiral, which is due to both the magnitude and the phase differences of particle ensemble acceleration $\langle a_x(t)\rangle$ and $\langle a_z(t)\rangle$ over time.

ACKNOWLEDGMENTS

DZ, PW, and CL acknowledge the financial support from the National Natural Science Foundation of China (12202270, 11872281, 12272271, 12002242).

DATA AVAILABILITY STATEMENT

The data that support the findings of this study are available from the corresponding author upon reasonable request.

Appendix A: Simulation results with $W_2/W_1 = 2$

In the case of unequal molecular weight $W_1 \neq W_2$ between the two fluids, the mass fraction equation is coupled to other equations, in contrast to the equal molecular weight case where the equations are decoupled. However, from the simulation with $\mathcal{A} = 0.15$ and $W_2/W_1 = 2$ whose Y_1 visualizations are shown in figure 18 along with the results from the equal W case 2DlowAt, we can observe that the flow physics does not differ much between the two cases. The spiraling motion, the secondary RT instability inside the spiral, as well as the bubble reacceleration are clearly visible in the visualizations of the $W_2/W_1 = 2$ case. However, it is not appropriate to extrapolate this observation to cases where $W_1 \gg W_2$ or $W_2 \gg W_1$.

Appendix B: Details on the initial conditions

The unperturbed initial conditions of the three simulation cases at various Atwood numbers consists of 1D profiles of density, pressure, and temperature that are uniform along

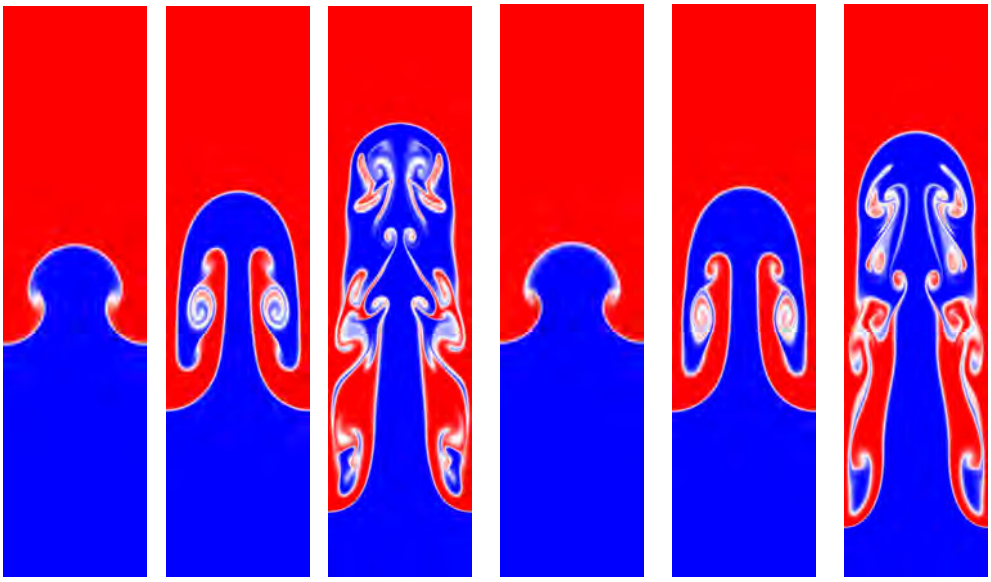

(a) (b) (c) (d) (e) (f)

FIG. 18. Panels (a)-(c) show the visualization of the Y_1 fields at non-dimensional time $\widehat{t} = 2.45, 3.67, 4.90$ for the 2DlowAt simulation in the paper. Panels (d)-(f) show the results from a low At simulation case with $W_1 : W_2 = 1 : 2$ and $\mathcal{A} = 0.15$ at the same instants.

the horizontal direction, while an initial perturbation is imposed on the quiescent vertical velocity field. We show the initial 1D profiles of the low, middle, and high $\mathcal{A}$ cases in figure 19. Inside the heavy and light fluids the densities are constant, with a density jump across the interface that is smoothed by a hyperbolic tangent function with a width approximately equals to $L_z/64$. The pressure and temperature fields in the heavy and light fluid phases are linear profiles so that the hydrostatic condition $dP/dz = -\rho g$ is satisfied and the temperature gradient $dT/dz = -g/R$ uniform across the domain.

The perturbation is imposed on the vertical velocity field with the form

$$u_z = u_p \cos\left(\frac{2\pi}{L_x}x\right) e^{-\frac{2\pi}{L_x}|z-z_0|\tanh\left(\frac{|z-z_0|}{L_x}\right)}$$

where u_p is a small quantity representing the initial perturbation magnitude chosen as $u_p = 0.005$ for the simulations performed in table I, L_x is the horizontal domain size, z_0 is the vertical coordinate of the interface. The exponential decaying quantity is to ensure the perturbation is localized near the interface.

The influence of perturbation magnitude u_p in single-mode RT is not important provided that the perturbed flow remains in the linear regime ($u_p \ll \sqrt{gL_x/10}$). We have tested

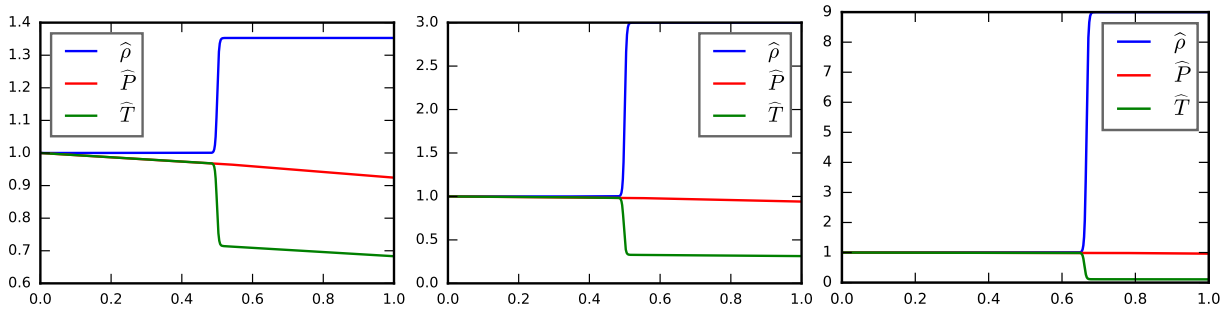

(a) $\mathcal{A} = 0.15$ (b) $\mathcal{A} = 0.5$ (c) $\mathcal{A} = 0.8$

FIG. 19. The one-dimensional profiles of the initial density, pressure, and temperature fields for the simulation cases with low, middle, and high Atwood numbers in panels (a), (b), and (c), respectively. The coordinate is normalized by L_z, while the density, pressure, and temperature fields are normalized by their respective values evaluated at $z = 0$. In the case $\mathcal{A} = 0.8$, the initial interface is chosen to locate at $2/3L_z$.

for the 2DlowAt case with a larger magnitude $u_p = 0.01$. Compared to $u_p = 0.005$ in the 2DlowAt case, the bubble and spike velocities are shown in figure 20. With a proper shift in time to account for the initial difference, the velocities of the bubble and the spike are very close between the two cases, indicating that the single-mode RT statistics is not sensitive to the initial perturbation magnitude.

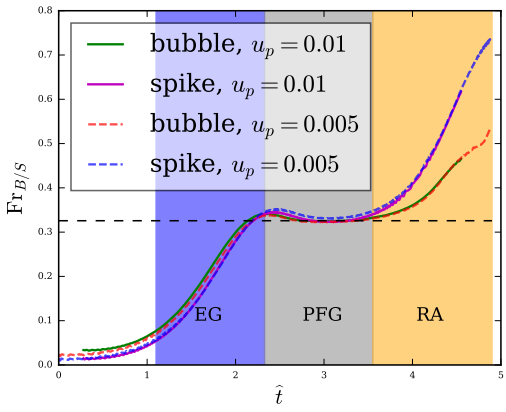

FIG. 20. Comparison of the bubble and spike Froude number (non-dimensional velocity) for the 2DlowAt case with perturbation magnitude $u_p = 0.005$ and 0.01. The $u_p = 0.01$ plots are shifted in time to have a fair comparison with the $u_p = 0.005$ case.

Appendix C: Correlation between trajectory curvature and acceleration

To corroborate the relationship between trajectory curvature and small scale quantities such as acceleration, we show in figure 21 the time history of particle trajectory curvature and the acceleration components that are tangent and normal to the instantaneous velocity:

$$\mathbf{a}_{\text{tangent}} = \frac{\mathbf{a}\cdot\mathbf{u}}{\|\mathbf{u}\|^2}\mathbf{u}; \quad \mathbf{a}_{\text{normal}} = \mathbf{a} - \mathbf{a}_{\text{tangent}}$$

Panels (a)-(c) are the results of one representative particle in each of the bubble, spike, and spiral ensembles, while panels (d)-(f) show the ensemble-averaged results. From visual inspection, the temporal evolution of curvature is closely correlated with the normal component of the acceleration a_{normal}, with high correlation coefficients as shown in the caption of figure 21, while the tangential acceleration component a_{tangent} captures the temporal fluctuations as in the evolution of curvature. This figure demonstrates that the trajectory curvature not only acts as a kinematic measure of local flow patterns, but also are closely connected to the dynamics of the flow.

---

[1] Rayleigh Rayleigh. Investigation of the character of the equilibrium of an incompressible heavy fluid of variable density. *Proceedings of the London mathematical society*, 1(1):170–177, 1882.

[2] Geoffrey Ingram Taylor. The instability of liquid surfaces when accelerated in a direction perpendicular to their planes. i. *Proceedings of the Royal Society of London. Series A. Mathematical and Physical Sciences*, 201(1065):192–196, 1950.

[3] Ye Zhou. Rayleigh–taylor and richtmyer–meshkov instability induced flow, turbulence, and mixing. i. *Physics Reports*, 720:1–136, 2017.

[4] W David Arnett, John N Bahcall, Robert P Kirshner, and Stanford E Woosley. Supernova 1987a. *Annual review of Astronomy and Astrophysics*, 27(1):629–700, 1989.

[5] R Betti and OA Hurricane. Inertial-confinement fusion with lasers. *Nature Physics*, 12(5):435, 2016.

[6] Huasen Zhang, Riccardo Betti, R Yan, D Zhao, D Shvarts, and H Aluie. Self-similar multimode bubble-front evolution of the ablative rayleigh-taylor instability in two and three dimensions. *Physical review letters*, 121(18):185002, 2018.

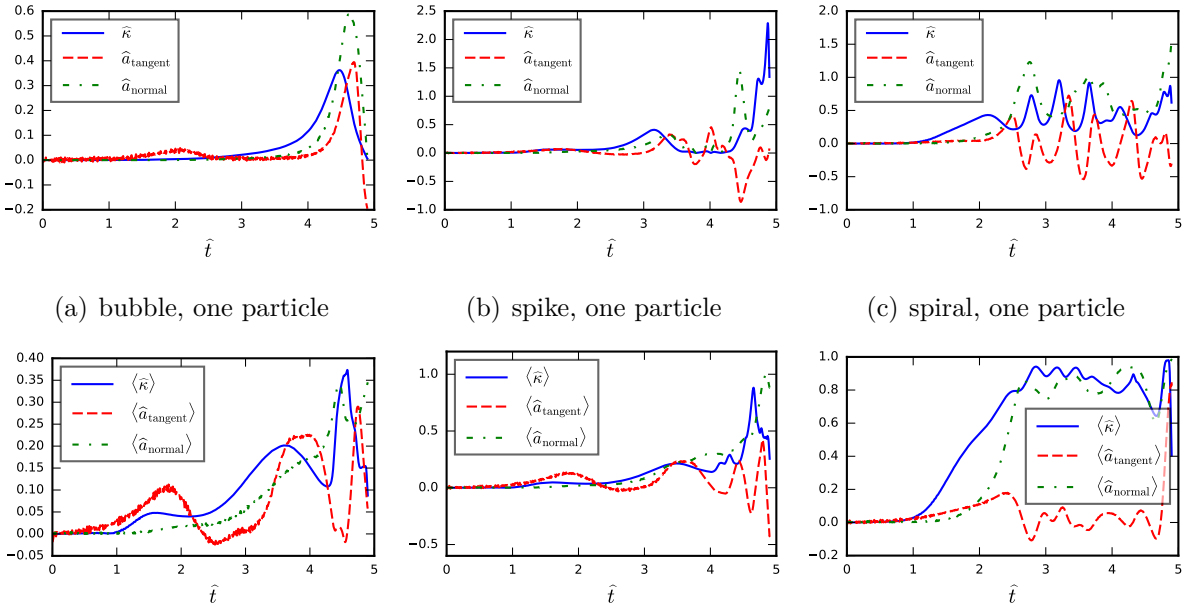

(a) bubble, one particle (b) spike, one particle (c) spiral, one particle

(d) bubble, mean (e) spike, mean (f) spiral, mean

FIG. 21. Panels (a)-(c), the temporal evolution of trajectory curvature κ, tangential and normal accelerations $a_{\text{tangent}}, a_{\text{normal}}$ for a single representative point in the bubble, spike, and spiral ensembles, respectively. The curvature is normalized by the domain size L_x, while accelerations are normalized by the gravity acceleration g. The correlation coefficients between κ and a_{normal} is 0.70, 0.77, 0.60 for the three panels. Panels (d)-(f), similar to (a)-(c), but show the mean value over the respective particle ensemble. The correlation coefficients between κ and a_{normal} is 0.93, 0.85, 0.86 for the three panels.

[7] H Zhang, R Betti, V Gopalaswamy, R Yan, and H Aluie. Nonlinear excitation of the ablative rayleigh-taylor instability for all wave numbers. *Physical Review E*, 97(1):011203, 2018.

[8] J Xin, R Yan, Z-H Wan, D-J Sun, J Zheng, H Zhang, H Aluie, and R Betti. Two mode coupling of the ablative rayleigh-taylor instabilities. *Physics of Plasmas*, 26(3), 2019.

[9] Huasen Zhang, R Betti, Rui Yan, and Hussein Aluie. Nonlinear bubble competition of the multimode ablative rayleigh–taylor instability and applications to inertial confinement fusion. *Physics of Plasmas*, 27(12), 2020.

[10] Jennifer C Beale and Rolf D Reitz. Modeling spray atomization with the kelvin-helmholtz/rayleigh-taylor hybrid model. *Atomization and sprays*, 9(6), 1999.

[11] Anqing Cui and Robert L Street. Large-eddy simulation of coastal upwelling flow. *Environmental Fluid Mechanics*, 4(2):197–223, 2004.

[12] Guido Boffetta and Andrea Mazzino. Incompressible rayleigh–taylor turbulence. *Annual Review of Fluid Mechanics*, 49:119–143, 2017.

[13] Ye Zhou. Rayleigh–taylor and richtmyer–meshkov instability induced flow, turbulence, and mixing. ii. *Physics Reports*, 723:1–160, 2017.

[14] Daniel Livescu. Turbulence with large thermal and compositional density variations. *Annual Review of Fluid Mechanics*, 52:309–341, 2020.

[15] Ye Zhou, Robin JR Williams, Praveen Ramaprabhu, Michael Groom, Ben Thornber, Andrew Hillier, Wouter Mostert, Bertrand Rollin, S Balachandar, Phillip D Powell, et al. Rayleigh–taylor and richtmyer-meshkov instabilities: A journey through scales. *Physica D: Nonlinear Phenomena*, page 132838, 2021.

[16] Tie Wei and Daniel Livescu. Late-time quadratic growth in single-mode rayleigh-taylor instability. *Physical Review E*, 86(4):046405, 2012.

[17] Xin Bian, Hussein Aluie, Dongxiao Zhao, Huasen Zhang, and Daniel Livescu. Revisiting the late-time growth of single-mode rayleigh–taylor instability and the role of vorticity. *Physica D: Nonlinear Phenomena*, 403:132250, 2020.

[18] Ge Zhang, Aiguo Xu, Dejia Zhang, Yingjun Li, Huilin Lai, and Xiaomian Hu. Delineation of the flow and mixing induced by rayleigh–taylor instability through tracers. *Physics of Fluids*, 33(7):076105, 2021.

[19] Raphael Zanella, György Tegze, Romain Le Tellier, and Hervé Henry. Two-and three-dimensional simulations of rayleigh–taylor instabilities using a coupled cahn–hilliard/navier–stokes model. *Physics of fluids*, 32(12), 2020.

[20] Hong Liang, Zhenhua Xia, and Haowei Huang. Late-time description of immiscible rayleigh–taylor instability: A lattice boltzmann study. *Physics of Fluids*, 33(8), 2021.

[21] JY Fu, HS Zhang, HB Cai, PL Yao, and SP Zhu. Effect of ablation on the nonlinear spike growth for the single-mode ablative rayleigh–taylor instability. *Matter and Radiation at Extremes*, 8(1), 2023.

[22] Tengfei Luo, Jianchun Wang, Chenyue Xie, Minping Wan, and Shiyi Chen. Effects of compressibility and atwood number on the single-mode rayleigh-taylor instability. *Physics of Fluids*, 32(1):012110, 2020.

[23] VN Goncharov. Analytical model of nonlinear, single-mode, classical rayleigh-taylor instability at arbitrary atwood numbers. *Physical review letters*, 88(13):134502, 2002.

[24] Sung-Ik Sohn. Simple potential-flow model of rayleigh-taylor and richtmyer-meshkov instabilities for all density ratios. *Physical Review E*, 67(2):026301, 2003.

[25] Wanhai Liu, Xiang Wang, Xingxia Liu, Changping Yu, Ming Fang, and Wenhua Ye. Pure single-mode rayleigh-taylor instability for arbitrary atwood numbers. *Scientific Reports*, 10(1):4201, 2020.

[26] Changwen Liu, Yousheng Zhang, and Zuoli Xiao. A unified theoretical model for spatiotemporal development of rayleigh–taylor and richtmyer–meshkov fingers. *Journal of Fluid Mechanics*, 954:A13, 2023.

[27] D Oron, L Arazi, D Kartoon, A Rikanati, U Alon, and D Shvarts. Dimensionality dependence of the rayleigh–taylor and richtmyer–meshkov instability late-time scaling laws. *Physics of Plasmas*, 8(6):2883–2889, 2001.

[28] P Ramaprabhu, Guy Dimonte, P Woodward, C Fryer, G Rockefeller, K Muthuraman, P-H Lin, and J Jayaraj. The late-time dynamics of the single-mode rayleigh-taylor instability. *Physics of Fluids*, 24(7):074107, 2012.

[29] Hussein Aluie, Shikhar Rai, Hao Yin, Aarne Lees, Dongxiao Zhao, Stephen M Griffies, Alistair Adcroft, and Jessica K Shang. Effective drift velocity from turbulent transport by vorticity. *Physical Review Fluids*, 7(10):104601, 2022.

[30] D Livescu. Numerical simulations of two-fluid turbulent mixing at large density ratios and applications to the Rayleigh-Taylor instability. *Philosophical Transactions of the Royal Society a-Mathematical Physical and Engineering Sciences*, 371(2003), 2013.

[31] Rui Wang, Yang Song, Zongqiang Ma, Yang Zhang, Jun Wang, Yaofeng Xu, Lili Wang, and Pei Wang. Scale-to-scale energy transfer in rarefaction-driven rayleigh–taylor instability-induced transitional mixing. *Physics of Fluids*, 35(2), 2023.

[32] Ze-Xi Hu, You-Sheng Zhang, Baolin Tian, Zhiwei He, and Li Li. Effect of viscosity on two-dimensional single-mode rayleigh-taylor instability during and after the reacceleration stage. *Physics of Fluids*, 31(10):104108, 2019.

[33] Scott A Wieland, Peter E Hamlington, Scott J Reckinger, and Daniel Livescu. Effects of isothermal stratification strength on vorticity dynamics for single-mode compressible rayleigh-taylor instability. *Physical Review Fluids*, 4(9):093905, 2019.

[34] Cheng-Quan Fu, Zhiye Zhao, Xin Xu, Pei Wang, Nan-Sheng Liu, Zhen-Hua Wan, and Xi-Yun Lu. Nonlinear saturation of bubble evolution in a two-dimensional single-mode stratified

compressible rayleigh-taylor instability. *Physical Review Fluids*, 7(2):023902, 2022.

[35] Cheng-Quan Fu, Zhiye Zhao, Pei Wang, Nan-Sheng Liu, Zhen-Hua Wan, and Xi-Yun Lu. Bubble re-acceleration behaviours in compressible rayleigh–taylor instability with isothermal stratification. *Journal of Fluid Mechanics*, 954:A16, 2023.

[36] Britton J Olson, Johan Larsson, Sanjiva K Lele, and Andrew W Cook. Nonlinear effects in the combined rayleigh-taylor/kelvin-helmholtz instability. *Physics of Fluids*, 23(11):114107, 2011.

[37] Feng Chen, Aiguo Xu, Yudong Zhang, and Qingkai Zeng. Morphological and non-equilibrium analysis of coupled rayleigh–taylor–kelvin–helmholtz instability. *Physics of Fluids*, 32(10):104111, 2020.

[38] Arash Hamzehloo, Paul Bartholomew, and Sylvain Laizet. Direct numerical simulations of incompressible rayleigh–taylor instabilities at low and medium atwood numbers. *Physics of Fluids*, 33(5):054114, 2021.

[39] Paul E Dimotakis. Turbulent mixing. *Annu. Rev. Fluid Mech.*, 37:329–356, 2005.

[40] Federico Toschi and Eberhard Bodenschatz. Lagrangian properties of particles in turbulence. *Annual review of fluid mechanics*, 41:375–404, 2009.

[41] Markus Holzner, Alex Liberzon, Nikolay Nikitin, Beat Lüthi, Wolfgang Kinzelbach, and Arkady Tsinober. A lagrangian investigation of the small-scale features of turbulent entrainment through particle tracking and direct numerical simulation. *Journal of Fluid Mechanics*, 598:465–475, 2008.

[42] II Wertgeim, MA Zaks, RV Sagitov, and AN Sharifulin. Instabilities, bifurcations, and nonlinear dynamics in two-dimensional generalizations of kolmogorov flow. *Fluid Dynamics*, 57(4):430–443, 2022.

[43] Hiroki Michioka and Ikuro Sumita. Rayleigh-taylor instability of a particle packed viscous fluid: Implications for a solidifying magma. *Geophysical research letters*, 32(3), 2005.

[44] Yi-Ju Chou and Yun-Chuan Shao. Numerical study of particle-induced rayleigh-taylor instability: Effects of particle settling and entrainment. *Physics of Fluids*, 28(4):043302, 2016.

[45] Marta Magnani, Stefano Musacchio, and Guido Boffetta. Inertial effects in dusty rayleigh–taylor turbulence. *Journal of Fluid Mechanics*, 926, 2021.

[46] Nitesh Attal and Praveen Ramaprabhu. The stability of reacting single-mode rayleigh–taylor flames. *Physica D: Nonlinear Phenomena*, 404:132353, 2020.

[47] Andrew W Cook. Enthalpy diffusion in multicomponent flows. *Physics of Fluids*, 21(5):055109, 2009.

[48] Dongxiao Zhao and Hussein Aluie. Inviscid criterion for decomposing scales. *Physical Review Fluids*, 3(5):054603, 2018.

[49] Dongxiao Zhao, Riccardo Betti, and Hussein Aluie. Scale interactions and anisotropy in rayleigh–taylor turbulence. *Journal of Fluid Mechanics*, 930, 2022.

[50] Richard Courant, Kurt Friedrichs, and Hans Lewy. Über die partiellen differenzengleichungen der mathematischen physik. *Mathematische annalen*, 100(1):32–74, 1928.

[51] Dongxiao Zhao and Hussein Aluie. Measuring scale-dependent shape anisotropy by coarse-graining: Application to inhomogeneous rayleigh-taylor turbulence. *arXiv preprint arXiv:2307.08918*, 2023.

[52] Wolfgang Braun, Filippo De Lillo, and Bruno Eckhardt. Geometry of particle paths in turbulent flows. *Journal of turbulence*, (7):N62, 2006.

[53] SUSUMU HASEGAWA, KATSUNOBU NISHIHARA, and HITOSHI SAKAGAMI. Numerical simulation of mixing by rayleigh-taylor instability and its fractal structures. *Fractals*, 4(03):241–250, 1996.

[54] Thierry Poinsot and Denis Veynante. *Theoretical and numerical combustion*. RT Edwards, Inc., 2005.

[55] Yosuke Matsumoto and Masahiro Hoshino. Onset of turbulence induced by a kelvin-helmholtz vortex. *Geophysical Research Letters*, 31(2), 2004.

[56] Hyun Geun Lee and Junseok Kim. Numerical simulation of the three-dimensional rayleigh–taylor instability. *Computers & Mathematics with Applications*, 66(8):1466–1474, 2013.

[57] Oleg Schilling. Progress on understanding rayleigh–taylor flow and mixing using synergy between simulation, modeling, and experiment. *Journal of Fluids Engineering*, 142(12), 2020.

[58] James Glimm, Xiao-lin Li, and An-Der Lin. Nonuniform approach to terminal velocity for single mode rayleigh-taylor instability. *Acta Mathematicae Applicatae Sinica*, 18(1):1–8, 2002.

[59] P Ramaprabhu, Guy Dimonte, Yuan-Nan Young, AC Calder, and B Fryxell. Limits of the potential flow approach to the single-mode rayleigh-taylor problem. *Physical Review E*, 74(6):066308, 2006.